

1 **Development of the DO₃SE-Crop model to assess ozone effects on crop phenology,**
2 **biomass and yield.**

3 Pritha Pande¹; Sam Bland¹; Nathan Booth ²; Jo Cook²; Zhaozhong Feng³; Lisa Emberson².

4 ¹ Stockholm Environment Institute at York, Environment & Geography Dept., University of
5 York, YO10 5DD, UK

6 ² Environment & Geography Dept., University of York, YO10 5DD, UK

7 ³ Key Laboratory of Agrometeorology of Jiangsu Province, School of Ecology and Applied
8 Meteorology, Nanjing University of Information Science & Technology, Nanjing, China.

9 Correspondence to: Pritha Pande (pritha.pande@york.ac.uk)

10 **Abstract**

11 A substantial body of empirical evidence exists to suggest that elevated O₃ levels are causing
12 significant impacts on wheat yields at sites representative of highly productive arable regions around
13 the World. Here we extend the DO₃SE model (designed to estimate total- and stomatal-O₃
14 deposition for risk assessment) to incorporate a coupled A_{net} - g_{sto} model to estimate O₃ uptake, an O₃
15 damage module (that impacts instantaneous A_{net} and the timing and rate of senescence), and a crop
16 phenology, carbon allocation, and growth model based on the JULES-Crop model. The model
17 structure allows scaling from the leaf to the canopy to allow for multiple leaf populations and
18 canopy layers. The DO₃SE-Crop model is calibrated and parametrised using O₃ fumigation data from
19 Xiaoji, China, for the year 2008 and for an O₃ tolerant and sensitive cultivar. The calibrated model
20 was tested on data for different years (2007 and 2009) and for two additional cultivars and was
21 found to simulate key physiological variables, crop development, and yield with a good level of
22 accuracy. The DO₃SE-Crop model simulated the phenological stages of crop development under
23 ambient and elevated O₃ treatments for the test datasets with an R² of 0.95 and an RMSE of 2.5
24 days. The DO₃SE-Crop model was also able to simulate O₃-induced yield losses of ~11-19 %
25 compared to observed yield losses of 12-34 %, with an R² of 0.68 (n=20) and an RMSE of 76 g/m².
26 Additionally, our results indicate that the variance in yield reduction is primarily attributed to the
27 premature decrease in carbon assimilation to the grains caused by accelerated leaf senescence,
28 which is brought forward by 3-5 days under elevated O₃ treatments.

29 Introduction

30 Ground-level ozone (O_3) is considered the most critical air pollutant causing global damage to
31 agricultural crops. Elevated O_3 concentrations are particularly problematic in Asia, where decades of
32 rapid economic growth, industrialisation, and urbanisation have seen sharp rises in pollutant
33 emissions associated with burning fossil fuels (Lin et al., 2017) causing substantial O_3 -induced crop
34 yield losses across the region (Feng et al., 2022). At the same time, climate change is considered a
35 substantial threat to arable productivity through changes in average and extreme temperature and
36 precipitation profiles across the region (IPCC, 2021). Reductions in precipitation are considered
37 responsible for poor harvests in recent years (Liu et al., 2010), and rising temperatures that reduce
38 the length of the crop growing season are thought to have caused losses in crop yield (Malhi et al.,
39 2021). There is now substantial evidence showing that stresses from O_3 pollution and climate
40 variability interact, causing either additive, synergistic, or antagonistic responses in crop
41 development, growth, and yield (Sillmann et al., 2021). The threat posed by these stresses is a
42 particular cause for concern in Asia since the continent contributes approximately 43% of the global
43 wheat production, with China contributing the highest production levels at 17% of the global wheat
44 supply (Feng et al., 2021). O_3 levels are rising substantially in important wheat-growing areas in
45 China such as the North China Plain and the Yangtze River Delta (Li et al., 2020; Zhang et al., 2023).
46 Concern over O_3 impacts led to the implementation in 2013 of a range of policies to try to reduce O_3
47 precursor emissions across China. These included a comprehensive management plan to control
48 volatile organic compounds (VOCs) from key industries, an atmospheric pollution prevention and
49 control law of the People's Republic of China and, a 2020 VOCs Management Plan (Li et al., 2021). As
50 a result, nitrogen oxide (NO_x) emissions, an important O_3 precursor, have decreased by 21% from
51 2013 to 2017 (Li et al., 2021). By contrast, VOCs have only slightly decreased by 2% over the same
52 period. Since China has a VOC limited O_3 regime, the reductions in NO_x lead to rather insignificant
53 changes in O_3 concentration (Li et al., 2021) though evidence suggests that reductions in O_3 may be
54 higher in rural than urban areas (Lee et al., 2020). This implies future policies to tackle ground level
55 O_3 pollution in China need to increase their focus on reducing VOCs along with NO_x (Lee et al., 2020)
56 and also emphasise the importance of being able to make assessments of O_3 damage to key
57 receptors such as staple crops.

58 At present, methods to assess the risk to crop productivity from changes in O_3 and climate variables
59 use a variety of different O_3 risk assessment methods (Ronan et al., 2020) and crop models as
60 discussed in depth in Emberson et al. (2018). In the past, O_3 risk assessment methods relied heavily
61 on dose-response relationships, empirically derived relationships that assess changes in a response
62 variable (most commonly yield) against an O_3 exposure metric (concentration or, more recently, flux-
63 based indices) (Pleijel et al., 2022). By contrast, methods to assess the impact of climate variables
64 (most commonly changes in temperature, precipitation and CO_2 concentration) tend to use crop
65 models since these allow the integration of the combined effect of a number of different variables
66 acting simultaneously to affect crop development, growth and yield (Schauberger et al., 2019). A
67 new generation of crop models that include O_3 damage are now being developed and applied and
68 have the potential to estimate the combined effect of O_3 and climate variables on crop
69 development, biomass and yield. Such models can arguably be classified into two types of crop
70 model. Firstly, those that rely on O_3 metrics (e.g. AOT40 or M7) to modify crop growth determined
71 by radiation use efficiency (Guarin et al., 2019; 2024) or evapotranspiration (Droustas et al., 2020).
72 Secondly, those that estimate stomatal O_3 uptake to modify crop growth determined by
73 photosynthesis and subsequent carbon assimilation (Tao et al., 2017; Schauburger et al., 2019;
74 Nguyen et al., 2024). The DO_3SE -Crop model falls into the latter category of photosynthetic-based
75 crop models and was developed to bridge the gap between O_3 risk assessment modelling methods
76 and crop models.

77 The DO_3SE model is an O_3 deposition model that can be embedded within atmospheric chemistry
78 transport models (e.g. Simpson et al., 2012) and uses either a multiplicative or coupled $A_{net}-g_{sto}$

79 model to estimate stomatal O₃ flux (Pande et al., 2024). Accumulated stomatal O₃ flux has been
80 successfully used as a damage metric (PODy - Phytotoxic Ozone Dose over a threshold y (LRTAP,
81 2017)) to predict O₃-induced yield loss (Pande et al., 2024). The ability of the DO₃SE model to
82 simulate A_{net} , and the inclusion of a process-based O₃ damage module for both instantaneous A_{net}
83 and early and enhanced senescence (after Ewert and Porter (2000)) lends itself to the development
84 of the DO₃SE model as a process-based crop model. The inclusion of resistance algorithms that can
85 assess the transport of O₃ concentrations from a reference height above a canopy down to the
86 canopy top, means the model can be embedded within existing atmospheric chemistry transport
87 schemes and hence applied for regional or global scale O₃ risk assessment whilst also modelling O₃
88 deposition. A comparison of the coupled stomatal A_{net} - g_{sto} model with the multiplicative g_{sto} model
89 within the DO₃SE framework has been made in Pande et al. (2024) and showed that the A_{net} - g_{sto}
90 model performed equally well, if not better, when used to develop O₃ dose-response relationships
91 for European wheat. This provides evidence of the suitability of the new photosynthetic based g_{sto}
92 model in DO₃SE.

93
94 In this study, we describe the development of a new DO₃SE-Crop model which builds on the
95 modified stomatal deposition component of the DO₃SE model (Pande et al. 2024) so that both CO₂
96 uptake for carbon assimilation as well as O₃ uptake via the stomata can be modelled consistently.
97 Further, we have incorporated the UK JULES crop model (Osborne et al., 2015) to allocate
98 assimilated carbon to plant components (roots, leaves, stems and harvest organs) according to crop
99 development stage. We also take account of the modifying effect of O₃ on instantaneous A_{net} as well
100 as accumulated A_{net} via O₃ effects on the onset and rate of leaf senescence and timing of crop
101 maturity through incorporation of algorithms developed by Ewert and Porter (2000). The UK JULES
102 crop model is used since this is the UK land surface exchange scheme in the UK Earth System Model
103 (UKESM) (Osborne et al., 2015) which has recently been developed to include exchange and impact
104 of trace gases (including O₃) along with other biogeochemical cycling between the atmosphere and
105 the land surface (Leung et al., 2020). This would in the future allow comparison of the UK JULES Crop
106 model, which uses O₃ mechanisms that modify instantaneous A_{net} to mimic changes in yield
107 consistent with flux-response relationships (Sitch et al., 2007), with the alternative O₃ damage
108 mechanisms used within DO₃SE-Crop.

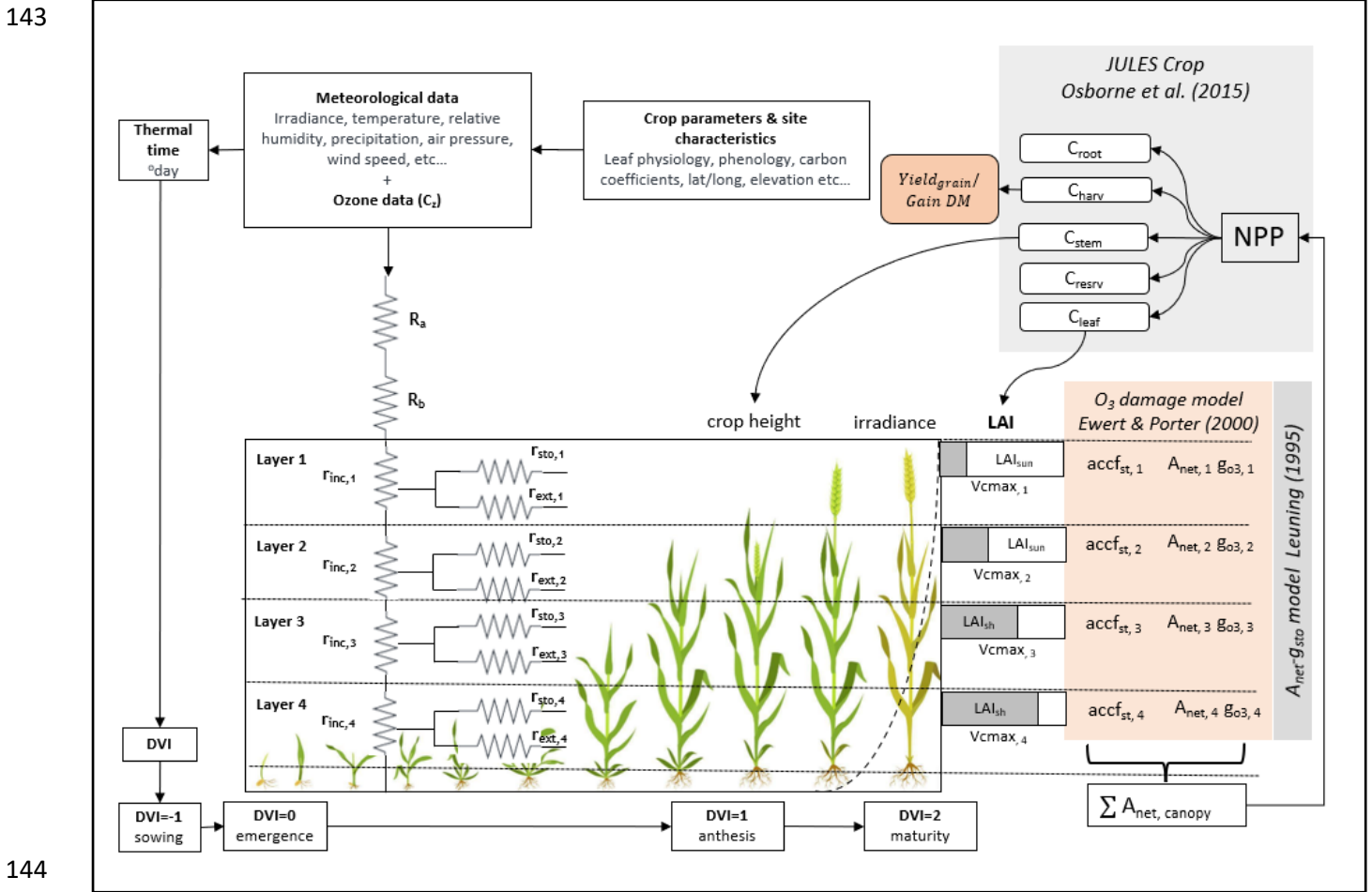
109 Here, we calibrate and evaluate the DO₃SE-Crop model using an experimental FACE dataset collected
110 in Xiaoji, China. This allows us to investigate the ability of the model to simulate O₃ damage for a
111 comparable agro-ecological region where crop productivity is severely threatened by both O₃
112 pollution and climate change. The key objectives of the paper are to assess the ability of DO₃SE-Crop
113 to simulate i). key phenological stages, ii) the relationship between leaf-level physiological variables
114 and within canopy O₃ concentrations, iii) C allocation to different parts of the crop and iv) O₃ induced
115 yield losses for tolerant and sensitive cultivars.

116 Methods

117 1. DO₃SE-Crop Model

118 Here we describe the development of the DO₃SE-Crop model (version 4 (V4.39.19)) for wheat
119 (*Triticum aestivum*) which is widely considered to be one of the most sensitive staple crops to O₃
120 (Feng et al., 2018). The key components of DO₃SE-Crop are illustrated in Fig.1. The model integrates
121 meteorological data, crop parameters, and site characteristics to simulate the impact of O₃ on crop
122 yield. Model inputs are irradiance, temperature, relative humidity, precipitation, air pressure, wind
123 speed, and O₃ concentration at a reference height (C_z) to calculate atmospheric resistances (R_a) and
124 boundary layer resistances (R_b) for O₃ deposition to the crop canopy. It further incorporates crop-
125 specific parameters related to leaf physiology, phenology and carbon coefficients, alongside site-
126 specific data (latitude, longitude and elevation) to simulate crop growth at stages from sowing to
127 maturity, denoted by the Development Vegetative Index (DVI). The canopy is divided into four
128 vertical layers, each characterised by sunlit (LAI_{sun}) and shaded (LAI_{sh}) leaf area index, which
129 influence the photosynthetic capacity (V_{cmax}) and O₃ uptake in each layer. The model accounts for
130 in-canopy resistance (r_{inc}) and external resistance (r_{ext}) in each layer, affecting the O₃ flux ($accf_{st}$)
131 and its impact on net photosynthesis (A_{net}) and stomatal conductance (g_{o_3}). The
132 $A_{net}g_{sto}$ relationship is modeled using the Leuning model (1995). Damage from O₃ is estimated after
133 Ewert & Porter (2000) for different canopy layers, which are aggregated to give the overall O₃ impact
134 on canopy A_{net} which is integrated according to the JULES Crop model (Osborne et al., 2015), which
135 uses the daily accumulated canopy A_{net} to calculate the net primary productivity (NPP). The NPP is
136 then distributed as carbon to various parts of the crop (roots (C_{root}), stems (C_{stem}), leaves (C_{leaf}),
137 harvestable organs (C_{harv})). The C_{harv} provides the yield and grain dry matter; C_{leaf} the LAI and
138 C_{stem} the crop height. The DO₃SE-Crop model requires hourly input meteorological and O₃
139 concentration data which is used to produce output on either an hourly (i.e. leaf physiology and
140 short-term O₃ damage variables) or daily (i.e. phenology, soil moisture, long-term O₃ damage, C
141 allocation, biomass and yield variables) time step.

142 Fig. 1 Schematic of the DO₃SE-Crop model.



145 1.1 DO₃SE-Crop Phenology

146 The DO₃SE-Crop model uses thermal time to define the rate of crop development in relation to the
 147 timing of three key developmental stages, TT_{emr} (the period from sowing to emergence), TT_{veg} (the
 148 period of emergence to start of grain filling) and TT_{rep} (the period from the start of grain filling to
 149 maturity) based on the method of Osborne et al. (2015). Thermal time is calculated by accumulating
 150 an effective temperature (T_{eff}) using base (T_b), optimum (T_o) and maximum (T_m) cardinal
 151 temperatures as shown in eq. [1].

$$152 \quad T_{eff} = \begin{cases} 0 & \text{for } T_{air} < T_b \\ T_{air} - T_b & \text{for } T_b \leq T_{air} \leq T_o \\ (T_o - T_b) \left(1 - \frac{T_{air} - T_o}{T_m - T_o}\right) & \text{for } T_o < T_{air} < T_m \\ 0 & \text{for } T_{air} \geq T_m \end{cases} \quad [1]$$

153 Where, T_{air} is the surface air temperature in °C, T_{eff} is at a maximum when $T_{air} = T_o$, this point
 154 denotes the highest developmental rate. T_{eff} declines as the temperature falls or rises above T_o ,
 155 with a linear decrease in crop development. T_{eff} is zero, i.e. no development, when T_{air} falls below
 156 or rises above T_b and T_m respectively i.e. $T_m \leq T_{air} < T_b$. During the sowing to emergence phase,

157 development is dependent on T_b , whereas during the vegetative and reproductive phase,
 158 development depends on T_m or T_o .

159 Winter wheat requires vernalisation (a period of exposure to low temperature during germination to
 160 accelerate flowering). Vernalisation alters the length of TT_{veg} and hence flowering initiation, with
 161 subsequent effects on later growth stages such as heading. Vernalisation occurs when the minimum
 162 (VT_{min}) and maximum (VT_{max}) daily temperature is less than 15°C and 30°C respectively (Zheng et
 163 al., 2015). Accumulated vernalised days (V_{dd}) are calculated as the sum of vernalised and
 164 devernalised days from emergence to the start of anthesis (Zheng et al., 2015) as shown in eq. [2].

$$165 \quad V_{dd} = \sum(V - V_d), \text{ where} \quad [2]$$

$$166 \quad V = \left(1.4 - 0.778 \times T_{air}, 0.5 + 13.44 \frac{T_{air}}{(T_{max} - T_{min} + 3)^2}\right) \quad \text{for } VT_{max} < 30^\circ\text{C and } VT_{min} < 15^\circ\text{C}$$

$$167 \quad V_d = (\min(0.5(T_{max} - 30), V_{prev})) \quad \text{for } VT_{max} > 30^\circ\text{C and } V_{dd} < 10 \text{ days}$$

168 The vernalisation factor (VF) decreases from 1 to 0 as (V_{dd}) increases. VF depends on a cultivar-
 169 specific vernalisation coefficient (PIV) as described by eq. [3].

$$170 \quad VF = 1 - (0.0054545 \times PIV + 0.0003) * (50 - V_{dd}) \quad [3]$$

171 Photoperiod (PP) or day length also affects the occurrence and timing of the flowering stage and is
 172 calculated according to latitude using standard solar geometry to estimate daylength (Jones, 1992).
 173 The photoperiod factor (PF) represents the sensitivity to PP which decreases from 1 to 0 as the
 174 photoperiod shortens and is estimated according to a cultivar-specific photoperiod coefficient (PID)
 175 after Tao et al. (2012) as described in eq. [4].

$$176 \quad PF = 1 - \left[\left(\frac{PID}{10000}\right) \times (20 - PP)^2\right] \quad [4]$$

177 Crop development is related to the development index (DVI) after Osborne et al. (2015) which takes
 178 values of -1 upon sowing, 0 on emergence, 1 at anthesis and 2 at crop maturity. The DO₃SE-Crop
 179 model DVI equations have been modified from Osborne et al. (2015) to take account of the
 180 photoperiod and vernalisation for winter wheat (see eq. [5]); for spring wheat these factors are
 181 omitted.

$$182 \quad -1 \leq DVI < 0 \quad \text{for } TT_{eff} < TT_{emr}$$

$$183 \quad 0 \leq DVI < 1 \quad \text{for } TT_{emr} \leq TT_{eff} \times VF \times PF < TT_{veg} \quad [5]$$

$$184 \quad 1 \leq DVI \leq 2 \quad \text{for } TT_{veg} \leq TT_{eff} \leq TT_{rep}$$

185 DO₃SE-Crop allows for any number of representative leaf populations (pop) and canopy layers (n)
 186 to be defined over the course of the crop growing season by dividing leaf populations as they
 187 emerge evenly across the canopy layers defined by LAI . In this study, we used a single leaf
 188 population and 4 canopy layers (i.e. $pop = 1$; $n = 4$) for simplicity. The crop sowing is assumed to
 189 be at $DVI = -1$ (start of TT_{emr}) and emergence at $DVI = 0$ (start of TT_{veg}). The flag leaf is assumed to
 190 develop at $DVI=1$, at the commencement of TT_{rep} , marking the initiation of anthesis (A_{start} ,
 191 flowering) and flag leaf emergence, which typically occurs 4-5 days prior to the onset of anthesis and
 192 is further divided into expanding and senescing leaf periods (i.e. tl_{ep} and tl_{se}) with a default ratio of
 193 0.67 to 0.33 for each of these periods. Maturity is assumed at $DVI = 2$, at the end of TT_{rep} . The model
 194 allows estimation of the $PODy$ metric by accumulating stomatal O₃ flux from the start of anthesis to
 195 maturity. The total canopy-leaf life span (TT_{leaf}) of the crop is distributed over the DVI between 0

196 and 2. The total lifespan (T_l) covers the full period from sowing to maturity, corresponding to DVI
 197 between -1 to 2. The relationship between these different variables is described in Fig. 2.

198 1.2 DO₃SE-Crop leaf-level physiology

199 Key leaf-level physiological variables of the DO₃SE-Crop model are A_{net} and g_{sto} . Net photosynthesis
 200 is simulated using the biochemical photosynthesis-based model initially developed by (Farquhar et
 201 al., 1980) and since modified by Sharkey et al. (2007). The coupled $A_{net}g_{sto}$ model of Leuning (1995)
 202 is used to estimate g_{sto} from A_{net} which means that g_{sto} is regulated by the demand of CO₂ for
 203 A_{net} on consideration of environmental conditions and crop physiology. Ozone stress, causing both
 204 instantaneous effects on A_{net} and long-term effects on A_{net} via leaf senescence is simulated based
 205 on algorithms developed by Ewert and Porter (2000).

206 1.2.1 Leaf net photosynthesis (A_{net})

207 The A_{net} model assumes that photosynthesis is constrained depending on prevailing environmental
 208 conditions according to three main mechanisms: Rubisco activity (A_c); ribulose-1,5-bisphosphate
 209 (RuBP) regeneration, which is constrained by the speed of electron transport (A_j); and the low rate
 210 of transfer of photosynthetic products (most frequently triose phosphate consumption) (A_p)
 211 (Sharkey et al., 2007) and by soil water stress (f_{PAW}); the algorithm for A_c which is based on Medlyn
 212 et al. (2002) and modified in DO₃SE-Crop to include the O₃ damage functions is given in eq. [6].

$$213 \quad A_c = V_{Cmax} \times f_{PAW} \times \frac{(C_i - \Gamma^*) \times f_{O_{3,s}}(d) \times f_{LS}}{C_i + K_c \left(1 + \frac{O_i}{K_o}\right)} \quad [6]$$

214 where V_{Cmax} ($\mu\text{mol CO}_2 \text{ m}^{-2}\text{s}^{-1}$) is the maximum carboxylation capacity at 25°C, C_i ($\mu\text{mol mol}^{-1}$) and
 215 O_i (mmol mol^{-1}) are the intercellular CO₂ and O₂ partial pressures; K_c ($\mu\text{mol mol}^{-1}$) and K_o (mmol
 216 mol^{-1}) are the Rubisco Michaelis-Menten constants for CO₂ and O₂; Γ^* ($\mu\text{mol mol}^{-1}$) is the CO₂
 217 compensation point in the absence of respiration; $f_{O_{3,s}}(d)$ is the factor that accounts for the
 218 cumulative stomatal O₃ flux effect on V_{Cmax} over the course of a day and; f_{LS} is the factor that
 219 accounts for the cumulative stomatal O₃ flux effect over the course of a leaf life span on leaf
 220 senescence. Section 1.2.1.1 gives a full description of the methods used to estimate O₃ damage. The
 221 f_{PAW} factor is calculated by eq. [7].

$$222 \quad f_{PAW} = 1 \quad \text{for } PAW_t \leq PAW \leq 100\%, \quad [7]$$

$$223 \quad f_{PAW} = 1 + \left\{ \frac{PAW / PAW_t}{PAW_t} \right\} \quad \text{for } PAW \leq PAW_t$$

224 PAW is the amount of water in the soil (in % terms) which is available to the plant estimated
 225 according to the DO₃SE models single soil layer bucket model (Bueker et al., 2012). At $PAW=100\%$
 226 the soil is at field capacity, at $PAW=0\%$ the soil is at wilting point. PAW_t is the threshold PAW , above
 227 which it is assumed there is no constraint on A_c , defined as 50% after LRTAP (2017). Only once PAW
 228 $< PAW_t$ will soil water begin to limit g_{sto} and hence stomatal O₃ flux.

229 The constraint on photosynthesis due to the rate of electron transport A_j is described in eq. [8].

$$230 \quad A_j = J \times \frac{C_i - \Gamma^*}{a \times C_i + b \times \Gamma^*} \quad [8]$$

231 where J is the electron transport rate ($\mu\text{mol CO}_2 \text{ m}^{-2}\text{s}^{-1}$), the parameters a and b denote the electron
 232 requirements for the formation of NADPH and ATP respectively (Sharkey et al., 2007)

233 Finally, the photosynthesis limitation due to the low rate of transfer of photosynthetic products A_p
 234 ($\mu\text{mol CO}_2 \text{ m}^{-2}\text{s}^{-1}$) is given in eq. [9].

$$235 \quad A_p = 0.5 \times V_{cmax} \quad [9]$$

236 The leaf net photosynthesis (A_{net}) in $\mu\text{mol CO}_2 \text{ m}^{-2}\text{s}^{-1}$ is calculated by eq. [10]

$$237 \quad A_{net} = (A_c, A_j, A_p) - R_d \quad [10]$$

238

239 Where leaf dark respiration (R_d) in $\mu\text{mol CO}_2 \text{ m}^{-2}\text{s}^{-1}$ is calculated as $V_{cmax} \times R_{dcoeff}$ where R_{dcoeff}
 240 is the leaf dark respiration coefficient initially set equal to 0.015 after Clark et al. (2011), a value
 241 provided for C3 grasses.

242 **1.2.1.1 Short- and long-term O₃ damage to A_c**

243 The short-term impact of O₃ on A_c is calculated according to the $f_{O_{3,s}}(d)$ factor (between 0 and 1)
 244 which allows for an instantaneous effect of O₃ on photosynthesis when stomatal O₃ flux (f_{st}), in
 245 $\text{nmol O}_3 \text{ m}^{-2} \text{ s}^{-1}$ calculated as described later in section 1.2.3, overwhelms detoxification and repair
 246 mechanisms (Betzberger et al., 2012; Feng et al., 2022), and is estimated following Ewert and
 247 Porter (2000). Here, $f_{O_{3,s}}(h)$ represents the relationship between f_{st} and a potential decrease in A_c
 248 calculated for every hour of the day by eq. [11].

$$249 \quad f_{O_{3,s}}(h) = 1 ; \quad \text{for } f_{st} \leq \frac{\gamma_1}{\gamma_2}$$

$$250 \quad f_{O_{3,s}}(h) = 1 + \gamma_1 - \gamma_2 \times f_{st} \quad \text{for } \frac{\gamma_1}{\gamma_2} < f_{st} < \frac{1+\gamma_1}{\gamma_2} \quad [11]$$

$$251 \quad f_{O_{3,s}}(h) = 0 ; \quad \text{for } f_{st} \geq \frac{1+\gamma_1}{\gamma_2}$$

252 where γ_1 (dimensionless) and γ_2 ($\text{nmol O}_3 \text{ m}^{-2} \text{ s}^{-1}$)⁻¹ are both short-term O₃ damage coefficients,
 253 with γ_1 representing the O₃ detoxification threshold below which no damage occurs to the
 254 photosynthetic system and γ_2 determines the effect of f_{st} on A_c once this detoxification threshold
 255 is exceeded; $f_{O_{3,s}}(d)$ and $f_{O_{3,s}}(d - 1)$ (i.e. $f_{O_{3,s}}(d)$ at the end of the previous day), are calculated
 256 by eq. [12].

$$257 \quad f_{O_{3,s}}(d) = f_{O_{3,s}}(h) \times r_{O_{3,s}} ; \quad \text{for } PAR \leq 50 \text{ W m}^{-2}$$

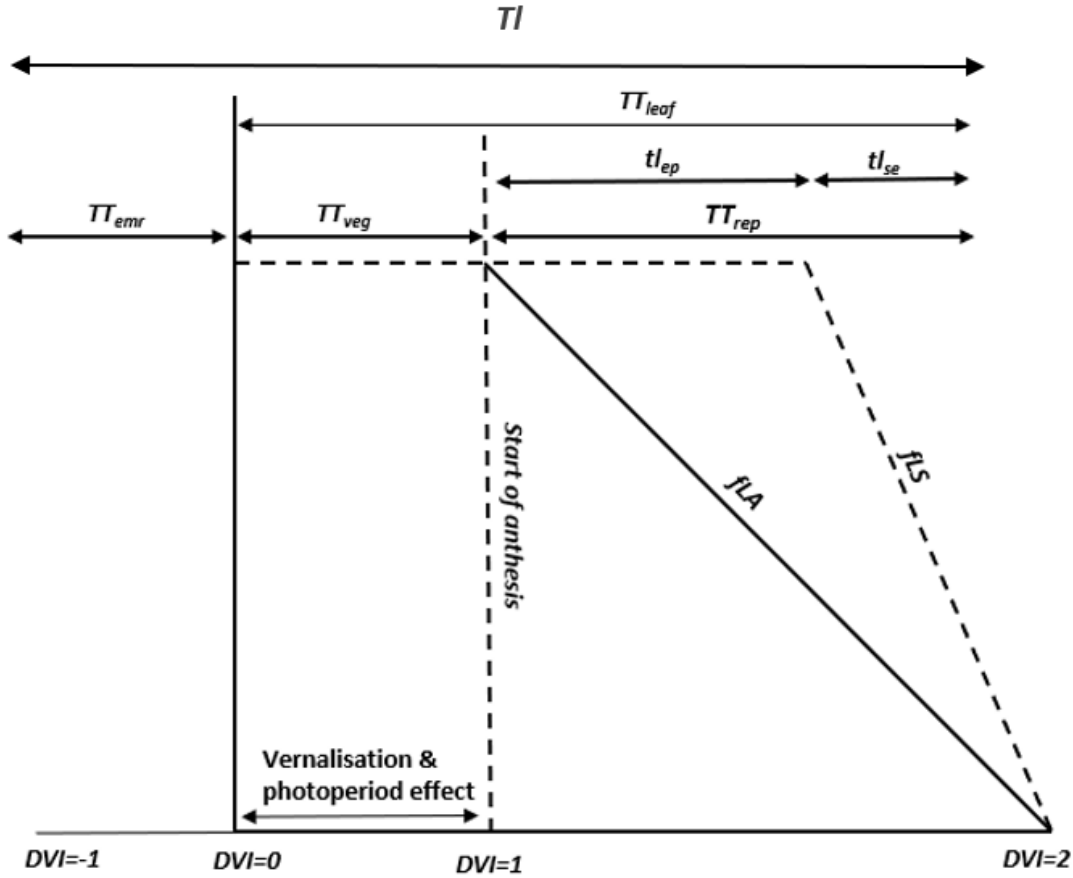
$$258 \quad f_{O_{3,s}}(d) = f_{O_{3,s}}(h) \times f_{O_{3,s}}(d - 1) \quad \text{for } PAR > 50 \text{ W m}^{-2} \quad [12]$$

259 where $r_{O_{3,s}}$ (dimensionless) represents incomplete recovery from O₃ overnight which depends on
 260 leaf age according to eq. [13].

$$261 \quad r_{O_{3,s}} = f_{O_{3,s}}(d - 1) + (1 - f_{O_{3,s}}(d - 1)) \times f_{LA} \quad [13]$$

262 The long-term impact of O₃ on V_{cmax} represented by the f_{LS} term represents the longer-term
 263 accumulation of stomatal O₃ flux (acc_{fst}) causing degradation to the Rubisco enzyme which triggers
 264 early and enhanced senescence of mature leaves (Gelang et al., 2000; Osborne et al., 2019). The
 265 acc_{fst} term is accumulated from 200°C days before anthesis until maturity to be consistent with the
 266 LRTAP (2017) which defines this as the O₃ sensitive period for wheat. The simulation of f_{LS} (and f_{LA}
 267 used in the short-term O₃ effect) are related to thermal time defined periods over the course of a
 268 leaf population life span TT_{leaf} as described in Fig. 2.

269 Fig 2. The division of thermal time defined periods (TT_{emr} , TT_{veg} , TT_{rep} and TT_{leaf} and the
 270 relationship with f_{LA} and f_{LS}) for the canopy, as represented in this study by a single leaf population.



271

272 The O_3 effect on f_{LS} is first simulated by estimating a weighted accumulated f_{st} ($fO3_l$) modified
 273 from Ewert and Porter (2000) by eq. [14].

$$274 \quad fO3_l = 1 - \max(\min(\gamma3 \times (acc_{fst} - CLsO3), 1), 0) \quad [14]$$

275 where $\gamma3$ determines the occurrence of senescence once a critical cumulative stomatal O_3 flux
 276 $CLsO3$ (in $mmol/m^2$) has been exceeded. The rate of senescence is determined by $\gamma4$, which
 277 determines the onset of senescence and $\gamma5$ which determines maturity as described in eq. [15]

$$278 \quad tl_{epO3} = tl_{ep} \times (1 - ((1 - fO3_l) \times \gamma4))$$

$$279 \quad tl_{seO3} = tl_{se} \times (1 - ((1 - fO3_l) \times \gamma5)) + zc \quad [15]$$

$$280 \quad zc = tl_{ep} - tl_{epO3}$$

281 Where tl_{ep} is the thermal time accumulated by a leaf (LTT) in $^{\circ}C$ days between a fully expanded leaf
 282 and the start of leaf senescence, tl_{epO3} is tl_{ep} with an O_3 effect which may bring senescence earlier,
 283 tl_{se} is the LTT in $^{\circ}C$ days between the onset of senescence and maturity and tl_{seO3} is tl_{se} with an O_3
 284 effect which may bring maturity earlier. f_{LS} is estimated by eq. [16].

$$285 \quad f_{LS} = 1; \quad \text{for } LTT \leq TT_{veg} + tl_{ep}$$

$$286 \quad f_{LS} = 1 - \frac{LTT - TT_{veg} - tl_{epO3}}{tl_{seO3}}; \quad \text{for } TT_{veg} + tl_{ep} < LTT < TT_{leaf}$$

287 $f_{Ls} = 0;$ *for* $LTT \geq TT_{leaf}$ [16]

288 **1.2.2 Stomatal conductance (g_{sto})**

289 The coupled photosynthesis-stomatal conductance ($A_{net}g_{sto}$) model based on Leuning (1995) and
 290 modified for vapour pressure deficit (VPD) is used to estimate g_{CO_2} , stomatal conductance to CO_2 in
 291 $\mu\text{mol } CO_2 \text{ m}^{-2} \text{ s}^{-1}$ as described in eq. [17].

292
$$g_{CO_2} = [f_{min} + m \times A_{net} \times f_{VPD} / (c_s - \Gamma)]$$
 [17]

293 where f_{min} ($\mu\text{mol } \text{m}^{-2} \text{ s}^{-1}$) is the minimum daytime g_{CO_2} (Leuning, 1990). The parameter m
 294 (dimensionless) is the composite sensitivity of g_{CO_2} to assimilation rate and vapour pressure deficit
 295 (VPD) with the relationship between VPD and relative stomatal conductance (f_{VPD}) estimated by
 296 eq. [18].

297
$$f_{VPD} = \left(1 + \left(\frac{VPD}{VPD_0}\right)^8\right)^{-1}$$
 [18]

298 where VPD_0 is an empirical parameter, defined using boundary line analysis, describing the variation
 299 in relative stomatal conductance with VPD (Danielsson et al., 2003; Pleijel et al., 2007). c_s (mmol
 300 mol^{-1}) is the external CO_2 concentration at the leaf surface and is calculated from the external CO_2
 301 concentration at the upper surface of the leaf boundary layer c_a ($\text{mmol } \text{mol}^{-1}$) so that

302 $c_s = c_a - \left(\frac{A_{net}}{g_{bCO_2}}\right)$ after Masutomi (2023) where g_{bCO_2} is the boundary layer conductance to CO_2 (in
 303 $\text{mol } \text{m}^{-2} \text{ s}^{-1}$), conversion factors for gases and heat across the boundary layer are given in S1a.

304 Finally, g_{CO_2} is converted to g_{O_3} in $\text{mmol } O_3 \text{ m}^{-2} \text{ s}^{-1}$ by dividing by 1000 and using the conversion
 305 factor 0.96 which assumes that the ratio of the diffusivities of gases in air are equal to the inverse of
 306 the square root of the ratio of molecular weights (as described in Campbell & Norman (1998)), see
 307 also supplementary S1b).

308 **1.2.3 Stomatal ozone flux (f_{st})**

309 Stomatal $[O_3]$ flux (f_{st} in $\text{nmol } \text{m}^{-2} \text{ s}^{-1}$) is calculated after the method described in the UNECE
 310 Mapping Manual (LRTAP, 2017) described in eq. [19].

311
$$f_{st} = C_l \times g_{O_3m/s} \times \frac{r_c}{r_{b,O_3} + r_c}$$
 [19]

312 Where C_l is the $[O_3]$ at the upper surface of the laminar layer of a leaf ($\text{nmol } O_3 \text{ m}^{-3}$). Ozone
 313 concentration in ppb can be converted to $\text{nmol } \text{m}^{-3}$ by multiplying O_3 in ppb by $P/(R \times T_{air,k})$ where
 314 P is the atmospheric pressure (1.013×10^5 in Pascal), R is the universal gas constant (8.31447
 315 J/mol/K) and $T_{air,k}$ is surface air temperature in degrees Kelvin. To convert g_{O_3} ($\text{mol } O_3 \text{ m}^{-2} \text{ s}^{-1}$) to
 316 $g_{O_3m/s}$ (m/s) we assume a standard temperature (20°C) and P , divide by 41 to give the conductance
 317 value in m/s . The $r_c/(r_{b,O_3} + r_c)$ term represents the O_3 deposition rate to the leaf through resistances
 318 r_b (the quasi-laminar resistance (s/m)) and r_c (the leaf surface resistance (s/m)) which allow for both
 319 stomatal and non-stomatal deposition to the leaf surface. r_c is $1/(g_{O_3m/s} + g_{ext})$ where g_{ext} is
 320 $1/2500$ (s/m). r_{b,O_3} is estimated by eq. [20].

321
$$r_{b,O_3} = 1.3 \times 150 \times \sqrt{\frac{L}{u_l}}$$
 [20]

322 Where the factor 1.3 accounts of the differences in diffusivity between heat and O_3 (see S1a), L is
 323 the cross wind leaf dimension (m) and u_l is the windspeed (m/s) at the top of the leaf laminar

324 boundary layer. The leaf boundary layer resistance to CO₂ is estimated using a value of 1.24 for the
 325 difference between heat and CO₂ in place of the 1.3 value for O₃ (Campbell and Norman, 1998).

326 1.3 DO₃SE-Crop canopy

327 The DO₃SE-Crop model uses a multi-layer approach to scale from leaf to the canopy. We assume that
 328 wind, irradiance, [O₃] concentration and leaf nitrogen content are the key environmental conditions
 329 which change with cumulative canopy leaf area index (*LAI*) and influence leaf physiology and
 330 therefore canopy layer estimates of A_{net} , g_{O_3} and g_{ext} ; other environmental variables (e.g., T_{air} and
 331 VPD) are assumed to remain constant over the canopy.

332 1.3.1 Canopy irradiance

333 Changes in irradiance through the canopy are described as sunlit and shaded canopy fractions and
 334 the associated quantity of direct and diffuse photosynthetically active radiation *PAR* (W/m²), these
 335 are estimated according to increasing levels of cumulative *LAI* using the methods of (Pury and
 336 Farquhar, 1997); full details are given in the section S2. Application of this method requires the
 337 canopy to be divided into layers of equal *LAI* (including both green (*LAI_G*) and brown (*LAI_B*) *LAI*).

338 *PAR* absorbed per unit leaf area is divided into PAR_{dir} , PAR_{diff} which also includes scattered (re-
 339 flected by the canopy) beam calculated by,

$$340 \quad PAR_{dir}(LAI) = (1 - \rho_{cb}(\beta)) k_b' I_b(0) \exp(-k_b' LAI) \quad [21]$$

$$341 \quad PAR_{diff}(LAI) = (1 - \rho_{cd}) k_d' I_d(0) \exp(-k_d' LAI) \quad [22]$$

342 Where; PAR_{dir} is the absorbed beam plus scattered beam PAR (Photosynthetically Active Radiation)
 343 per unit leaf area, PAR_{diff} is the absorbed diffuse plus scattered diffuse PAR per unit leaf area, ρ_{cb} is
 344 canopy reflection coefficient for beam PAR; ρ_{cd} is canopy reflection coefficient for diffuse PAR; k_b' is
 345 beam and scattered beam PAR extinction coefficient; k_d' is diffuse and scattered diffuse PAR
 346 extinction coefficient; β is the solar elevation above the horizontal plane of the Earth's surface; $I_b(0)$
 347 beam PAR per unit ground area at the top of the canopy; $I_d(0)$ is diffuse PAR per unit ground area at
 348 the top of the canopy.

349 Estimates of the *LAI* fractions of sunlit (LAI_{sun}) and shaded (LAI_{sh}) parts of each canopy layer (*i*)
 350 are made by eq. 23 and 24.

$$351 \quad LAI_{sun,i} = \left[1 - \exp\left(-0.5 \times \frac{LAI_i}{\sin\beta}\right) \right] \times 2\sin\beta \quad [23]$$

352 Where β is the solar elevation angle (see section S3)

$$353 \quad LAI_{sh,i} = LAI_i - LAI_{sun,i} \quad [24]$$

354 The DO₃SE-Crop model simulates *LAI* as part of the crop growth model and *LAI* is assumed to be
 355 evenly distributed across all layers (see section 1.4.2 and eq. 43).

356 Therefore, *PAR* for the sunlit part of each layer (PAR_{sun}) can be described as

$$357 \quad \int_{LAI_i}^{LAI_n} PAR_{sun} = \int_{LAI_i}^{LAI_n} (LAI_{sun,i}) \times (PAR_{sh} + PAR_{bsun}(\beta)) dLAI$$

358 Where; PAR_{sh} is absorbed PAR by shaded leaves per unit leaf area and PAR_{bsun} beam PAR
 359 absorbed by sunlit leaves per unit leaf area; and where $\int_{LAI_i}^{LAI_n} PAR_{dir}$ can be written as $(1 - \rho_{cb}$
 360 $(\beta)) \times k_b' \times I_b(0) \times [exp(-k_b' LAI_i) - exp(-k_b' LAI_n)]$ and $PAR_{bsun}(\beta) = (1 - \sigma) I_b(0) \frac{\cos\alpha_l}{\sin\beta}$

361 Where; α_l is angle of irradiance beam on the leaf normal; σ is leaf scattering coefficient for PAR

362 Similarly, PAR for the shaded part of each layer (PAR_{sun}) can be described as

$$363 \int_{LAI_i}^{LAI_n} PAR_{sh} = \int_{LAI_i}^{LAI_n} (LAI_{sh,i}) \times (PAR_{diff} + PAR_{bsun}) dLAI$$

364 Where $\int_{LAI_i}^{LAI_n} (PAR_{diff} (LAI))$ can be written as $(1 - \rho_{cd}) \times k_b' \times Ib(0) \times [exp(-k_d' LAI_i) -$
 365 $exp(-k_d' LAI_n)] dL$ and $\int_{LAI_i}^{LAI_n} PAR_{bs} (LAI)$ is $I_b(0) [PAR_{dir} - (1 - \sigma)k_b \times [exp(-k_b LAI_i) -$
 366 $exp(-k_b LAI_n)]$ and $PAR_{bs} (LAI)$ is absorbed scattered beam PAR per unit leaf area.

367 1.3.2 Canopy [O₃] concentration

368 O₃ concentration will vary as a function of O₃ loss to the canopy (i.e. deposition via the stomates and
 369 external plant parts) and O₃ replacement from ambient air concentrations above the canopy. Limited
 370 data have been collected showing how O₃ concentrations vary with canopy depth in semi-natural
 371 communities (Jaggi et al., 2006). These data suggest that a minimum, bottom canopy O₃
 372 concentration (C_{zb}), is about 0.2 times that at the top of the canopy (C_{zh}) and that the O₃
 373 concentration difference within the canopy is closely related to the LAI of the canopy layers.

374 Since each canopy layer can be assumed to be a parallel sink, the O₃ flux to a layer depends on the
 375 conductance (inverse of resistance) of that layer and the O₃ concentration at the top of the layer (C_i ;
 376 with C_0 being C_{zh} (i.e. the O₃ concentration at height C_h , the top of the canopy)); we follow and
 377 generalise the work of Waggoner (1971) by separating the canopy into nL leaf layers. We calculate
 378 the O₃ concentration for each layer, C_i , from O₃ intake, I_i , by;

$$379 C_i = r_{c,i} I_i \quad [25]$$

380 With $r_{c,i}$ the leaf surface resistance to O₃ for layer i . I_i is calculated as the solution to a system of
 381 linear equations. Relating $r_{c,i}$, I_i , and resistances of the bulk air among the leaves (R_i), the in-canopy
 382 aerodynamic resistance for layer i . Assuming above the canopy there is a uniform O₃ concentration
 383 C_0 , we use generalised equations from Waggoner (1971) for the difference in O₃ concentration
 384 between the exterior air and leaf interior, which for the top layer is C_0 minus 0, so C_0 and for each
 385 lower layer the difference is 0. This O₃ concentration difference is calculated by;

$$386 C_0 = R_i \sum_{j=1}^{nL} I_j + r_{c,1} I_1 \quad [26]$$

387 For the top canopy layer,

$$388 0 = R_i \sum_{j=i}^{nL} I_j + r_{c,i} I_i - r_{c,i-1} I_{i-1} \quad [27]$$

389 For each canopy layer i between the top layer and the bottom layer, and;

$$390 0 = R_{nL+1} I_{nL+1} - r_{c,nL} I_{nL} \quad [28]$$

391 For the bottom layer of the canopy, between the lowest leaf layer and the ground. These can also be
 392 written into the matrix form;

$$393 \begin{pmatrix} r_{c,1} + R_1 & R_1 & R_1 & \cdots & R_1 \\ -r_{c,1} & r_{c,2} + R_2 & R_2 & \cdots & R_2 \\ 0 & -r_{c,2} & r_{c,3} + R_3 & \cdots & R_3 \\ \vdots & \vdots & \vdots & \ddots & \vdots \\ 0 & 0 & 0 & \cdots & R_{nL+1} \end{pmatrix} \begin{pmatrix} I_1 \\ I_2 \\ I_3 \\ \vdots \\ I_{nL+1} \end{pmatrix} = \begin{pmatrix} C_0 \\ 0 \\ 0 \\ \vdots \\ 0 \end{pmatrix} \quad [29]$$

394 Which can be numerically solved for I_x when $r_{c,1} \neq 0$ and $R_1 \neq 0$.

395 Resistances for each layer are calculated as described in the supplementary material (section S5)
396 using standard DO₃SE deposition modelling methods (Emberson et al., 2012).

397 **1.3.3 Canopy maximum carboxylation capacity (V_{cmax})**

398 We allow for an exponential decrease in leaf N with canopy depth which will influence both the
399 photosynthetic capacity (V_{cmax}) and hence dark respiration (R_{dc}). Photosynthetic capacity at each
400 canopy layer i is calculated by eq. [30].

401

$$402 \quad V_{cmax,i} = n_e \times n_0 \times e^{-kN \left(\frac{LAI_i}{LAI}\right)} \quad [30]$$

403 Where n_e (mol CO₂ m⁻² s⁻¹ kg C (kg N)⁻¹) is a constant relating leaf nitrogen to Rubisco carboxylation
404 capacity, n_0 (kg N [kg C]⁻¹) is the leaf N concentration at the top of the canopy and kN is a nitrogen
405 profile co-efficient initially set at 0.78 after (Clark et al., 2011). The model assumes non-limiting
406 conditions for soil nitrogen, in accordance with the experimental data.

407 **1.3.4 Canopy Photosynthesis ($Anet_c$)**

408 Net canopy photosynthesis ($Anet_c$) determines the amount of C assimilated by the entire canopy
409 that can subsequently be allocated to different plant parts (i.e. less than the C respired for plant
410 growth and maintenance, see section 1.4.1), the amount of C assimilation will ultimately determine
411 whole plant biomass. The net photosynthesis for each canopy layer ($Anet_i$) is calculated according to
412 the LAI fraction of that layer that is sunlit ($LAI_{sun,i}$) and shaded ($LAI_{sh,i}$) within the layer (i),
413 multiplied by the net photosynthesis of the sunlit ($Anet_{sun,i,j}$) and shaded leaf ($Anet_{sh,i,j}$),
414 respectively described by eq. [31] and [32].

$$415 \quad Anet_i = LAI_{sun,i} \times Anet_{sun,i} + LAI_{sh,i} \times Anet_{sh,i} \quad [31]$$

416

417 with $Anet_c$ calculated by,

$$418 \quad Anet_c = \sum_{i=1}^n Anet_i \quad [32]$$

419 $Anet_c$ is converted from $\mu\text{mol CO}_2 \text{ m}^{-2} \text{ s}^{-1}$ to $\text{kg C m}^{-2} \text{ day}^{-1}$ by multiplying by 3600 (converting from
420 seconds to hours), multiplying by 1.2 (representing the kg of C per mol) and summing each hourly
421 $Anet_c$ over the course of a day. This $Anet_c$ is used in the equation 37.

422 **1.3.5 Canopy Stomatal Conductance (g_{O3_c})**

423 Similarly, canopy layer (i) stomatal conductance to O₃ (g_{O3_i}), which is converted from g_{CO_2} by
424 assuming a diffusivity ratio of 0.96 to convert from CO₂ to O₃ and is calculated by eq. [33] with whole
425 canopy stomatal conductance calculated by eq. [34].

$$426 \quad g_{O3_i} = LAI_{sun,i} \times g_{O3_{sun,i}} + LAI_{sh,i} \times g_{O3_{sh,i}} \quad [33]$$

$$427 \quad g_{O3_c} = \sum_{i=1}^n g_{O3_i} \quad [34]$$

428 This is converted from g_{O3_i} in eq. [33] by dividing the conductance value in $\text{mmol m}^{-1} \text{ s}^{-1}$ by 41000
429 (assuming standard temperature (20°C) and air pressure (1.013 x 10⁵ Pa)) to give conductance in
430 m/s.

431

432 1.4 Crop biomass, LAI, height and yield variables

433 The following section describes how to estimate crop biomass, important canopy characteristics
434 (*LAI* and crop height (*h*)) and yield variables from accumulated calculations of $Anet_c$ over the
435 course of the growing season following (Osborne et al., 2015).

436

437 1.4.1 Crop biomass (*NPP* and *GPP*)

438 The simulation of crop growth requires an estimate of the net primary productivity (*NPP*) which is
439 calculated at the end of each day and summed over the growing season. Carbon is assumed to be
440 allocated to five key crop components: root, leaf, stem, harvest, and reserve pools (Osborne et al.,
441 2015). This carbon allocation is ultimately used to simulate leaf area index (*LAI*), canopy height (*h*),
442 biomass, harvest index, and yield at the end of each day throughout the growing season.

443 Net primary productivity NPP ($\text{kg C m}^{-2} \text{ day}^{-1}$) is accumulated throughout the day using the JULES-
444 crop approach to model crop growth (Osborne et al., 2015) described in eq. [35].

$$445 \quad NPP = GPP - R_p \quad [35]$$

446 where GPP is the gross primary productivity ($\text{kg C m}^{-2} \text{ day}^{-1}$) and R_p is plant respiration divided into
447 maintenance (R_{pm}) and growth (R_{pg}) respiration ($\text{kg C m}^{-2} \text{ day}^{-1}$) (Clark et al., 2011) where $R_p =$
448 $R_{pm} + R_{pg}$ and where R_{pg} is assumed to be a fixed fraction of the NPP as shown in eq. [36].

$$449 \quad R_{pg} = R_{gcoeff} (GPP - R_{pm}) \quad [36]$$

450 Where R_{gcoeff} is the growth respiration co-efficient which was initially set to 0.25 based on the
451 value for all PFTs (i.e. forests and grasses including crops) in (Clark et al., 2011). GPP is calculated by
452 eq. [37].

$$453 \quad GPP = Anet_c + f_{PAW}R_{dc} \quad [37]$$

454 where $Anet_c$ is net canopy photosynthesis (see eq. 28) and $f_{PAW}R_{dc}$ is the soil-moisture modified
455 canopy dark respiration ($\text{kg C m}^{-2} \text{ day}^{-1}$) where $R_{dc} = V_{cmax,i} \times R_{dcoeff}$ with R_{dcoeff} initially
456 assumed to be 0.015 based on (Clark et al., 2011); $V_{cmax,i}$ is the maximum carboxylation efficiency
457 for each canopy layer i which decreases from the top to bottom of the canopy (see eq. 30) and
458 f_{PAW} is calculated in eq. [7].

459 Leaf maintenance respiration (R_{pm}) is assumed equivalent to the soil moisture modified canopy dark
460 respiration, while root and stem respiration are assumed to be independent of soil moisture but to
461 have the same dependencies on C content. We assume a fixed relationship between C and N
462 contents of these organs so that R_{pm} can be estimated by eq. [38].

$$463 \quad R_{pm} = R_{dc} \times (f_{sw} + (\frac{C_{root} + C_{stem}}{C_{leaf}})) \quad [38]$$

464 The C accumulating as NPP each day is divided into five carbon pools i.e. root (C_{root}), leaf (C_{leaf}),
465 stem (C_{stem}), reserve (C_{resv}), and harvest (C_{harv}) ($\text{kg C m}^{-2} \text{ day}^{-1}$) according to partition coefficients
466 (see eq. [39]) allowing for accumulation of C in these pools over the course of the crop growth
467 period.

$$468 \quad \frac{dC_{root}}{dt} = p_{root}NPP,$$

$$469 \quad \frac{dC_{leaf}}{dt} = p_{leaf}NPP,$$

$$470 \quad \frac{dC_{stem}}{dt} = p_{stem}NPP (1 - \tau), \quad [39]$$

$$471 \quad \frac{dC_{harv}}{dt} = p_{harv}NPP,$$

$$472 \quad \frac{dC_{resv}}{dt} = p_{stem}NPP, \tau$$

473 where τ is the fraction of stem C that is partitioned into the reserve pool. p_{root} , p_{leaf} , p_{stem} ,
 474 $p_{harv} = 1$. The partition coefficients are related to the crop development stage (DVI) and hence
 475 effective thermal time (TT_{eff}) since emergence. The partition coefficients are based on Osborne et
 476 al. (2015) and provided as a function of DVI using six parameters to continuously describe varying
 477 partition coefficients over the duration of the crop growing season. We use the same multinomial
 478 logistic as that described in (Osborne et al., 2015) to define this function according to eq. [40].

$$479 \quad p_{root} = \frac{e^{\alpha_{root} + (\beta_{root} DVI)}}{e^{\alpha_{root} + (\beta_{root} DVI)} + e^{\alpha_{stem} + (\beta_{stem} DVI)} + e^{\alpha_{leaf} + (\beta_{leaf} DVI)} + 1},$$

$$480 \quad p_{stem} = \frac{e^{\alpha_{stem} + (\beta_{stem} DVI)}}{e^{\alpha_{root} + (\beta_{root} DVI)} + e^{\alpha_{stem} + (\beta_{stem} DVI)} + e^{\alpha_{leaf} + (\beta_{leaf} DVI)} + 1},$$

$$481 \quad p_{leaf} = \frac{e^{\alpha_{leaf} + (\beta_{leaf} DVI)}}{e^{\alpha_{root} + (\beta_{root} DVI)} + e^{\alpha_{stem} + (\beta_{stem} DVI)} + e^{\alpha_{leaf} + (\beta_{leaf} DVI)} + 1}, \quad [40]$$

$$482 \quad p_{harv} = \frac{1}{e^{\alpha_{root} + (\beta_{root} DVI)} + e^{\alpha_{stem} + (\beta_{stem} DVI)} + e^{\alpha_{leaf} + (\beta_{leaf} DVI)} + 1},$$

483 Where DVI is the development index; α and β partition parameters. These parameters describe the
 484 shape of the thermal time varying partition coefficient for leaves, roots and stems.

485 Once C is no longer partitioned to stems, C from the stem reserve pool will mobilise to the harvest
 486 pool at a rate of 10% per day following (Osborne et al., 2015) described by eq. [41].

$$487 \quad C_{harv} = C_{harv} + (0.1 C_{resv}) C_{resv} = 0.9 C_{resv} \quad \text{for } p_{stem} < 0.01 \quad [41]$$

488 Total leaf C is divided between green leaf C ($C_{leaf,green}$), and brown leaf carbon ($C_{leaf,brown}$). Carbon
 489 from the $C_{leaf,green}$ will mobilise to the harvest pool at the rate of 5% per day after (Osborne et al.,
 490 2015) and to the $C_{leaf,brown}$ at a rate of 24% per day once $f_{LS} > 1$ as described in eq. [42]

$$491 \quad \{C_{harv} = C_{harv} + (0.05 C_{leaf,green}) C_{leaf,green} = 0.86 C_{leaf} \quad C_{leaf} = 0.86 C_{leaf,green} +$$

$$492 \quad 0.24 C_{leaf,brown} \} \text{ for } f_{LS} > 1 \quad [42]$$

493 1.4.2 Leaf area Index (LAI) and stem height (h)

494 At the end of each day, the C content of the stem and leaf is used to estimate LAI by eqs. [43] and
 495 [44].

$$496 \quad LAI = (C_{leaf} / f_c) \times SLA \quad [43]$$

$$497 \quad \text{where } SLA = \gamma (DVI + 0.06)^\delta \quad [44]$$

498 The values γ and δ were determined by fitting the values to the paired values of DVI and specific leaf
 499 area (SLA). The value of f_c is 0.5 (unitless), denotes carbon fraction of dry matter.

500 The amount of C in the stem is used to calculate the crop height h in m by eq. [45].

$$501 \quad h = k (C_{stem} / f_c)^\lambda \quad [45]$$

502 where k and λ were determined by fitting the value C_{stem} and h

503

504 1.4.3 Yield variables

505 According to (Osborne et al., 2015) yield can be calculated from the C allocated to the harvest pool
506 (C_{harv}) at the end of the growing season as described in eq. [46]

$$507 \text{Yield}_{grain} = \frac{(C_{harv} \times (1/f_c) \times D_w \times E_g)}{1000} \quad [46]$$

508 Where harvested C is converted to total biomass (using the conversion factor $f_c=0.5$), i.e., by
509 multiplying the harvested C by $1/f_c$, and then by $1/0.84$ (D_w) to account for the grain moisture
510 content (Mulvaney and Devkota, 2020). C_{harv} includes both chaff and grain however, O₃ fumigation
511 experimentalists tend to only include grain when calculating total crop yield at the end of the
512 growing season, so we assume 15% of the yield is chaff and include a grain to ear ratio, E_g , of 0.85.
513 Dividing by 1000 converts yield from kg C m⁻² to g C m⁻², the unit most often used to describe
514 experimental yield results.

515 Evaluation of the DO₃SE-Crop model uses a variety of growth 'dry matter (DM)' metrics. Some of the
516 most important metrics and their calculations are: 'Straw DM' which is calculated as the sum of
517 carbon allocated to C_{stem} , C_{leaf} , and C_{resv} ; 'Ear DM' is calculated from C_{harv} excluding the
518 moisture content (D_w) conversion; 'Grain DM' is calculated from C_{harv} excluding both the moisture
519 content (D_w) conversion and removing the chaff fraction conversion E_g ; 'Above ground DM' is the
520 straw DM plus the Ear DM; 'Below ground DM' is converted from C_{root} ; and 'Harvest index' is
521 the Gain DM divided by the Above ground DM. In all cases the f_c conversion factor is used to
522 convert from e.g. g C m⁻² to g DM m⁻².

523 2. DO₃SE-Crop model calibration

524 2.1 Xiaoji China experimental dataset

525 The DO₃SE-Crop model was used to analyse the O₃-FACE (Free Air Concentration Enrichment)
526 experimental data collected in Xiaoji, Jiangdu, Jiangsu Province, China. The wheat crop was grown in
527 fully open-air field conditions for three consecutive growing seasons from 2007 to 2009. The dataset
528 includes four modern cultivars of winter wheat (*Triticum aestivum* L.) grown under ambient (AA) and
529 elevated (E) O₃, with the elevated treatment being, on average, 25% above the ambient O₃
530 concentrations from early March/April to the end of May each year. The four cultivars were Yannong
531 19 (strong-gluten wheat, hereafter Y19), Yangmai 16 (medium-gluten wheat, hereafter Y16),
532 Yangmai 15 (weak-gluten wheat, hereafter Y15), and Yangfumai 2 (weak-gluten wheat, hereafter Y2)
533 (Zhu et al., 2011).

534 Soil water availability was sufficient for optimum wheat crop growth, so we assumed there was no
535 soil moisture stress (Feng et al., 2012). Any data gaps were filled following the AgMIP-O₃ gap filling
536 protocol (see S4). For large O₃ data gaps (i.e. greater than 2 weeks) occurring outside the O₃
537 fumigation period, we used scaled WFRChem (version 4.2) data for Xiaoji (Conibear et al., 2018) to
538 ensure consistency in model calibration and potential applications across China. The dataset
539 provides grain yield components, including the number of ears per square meter, the number of
540 grains per ear, and the grain dry matter (*Grain DM*, in g/m²) (Feng et al., 2011; 2016). Additional
541 physiological datasets (i.e. A_{net} , V_{cmax} , J_{max} , and g_{H2O} (converted to g_{O3} as described in S1b)) are
542 also provided, but only for the year 2008 for all cultivars (Y2, Y19, Y15, and Y16) and for the flag leaf.
543 The 2008 data also include measurements of the Chlorophyll (in mg m⁻²) which can be used to assess
544 the level of senescence experienced by the leaf Mariën et al. (2019). Since the year 2008 also

545 showed significant differences in *Grain DM* between AA and E O₃ treatments (a mean relative yield
 546 difference of 6.73 for all cultivars, see Table S2b) this year was used to train the DO₃SE-Crop model
 547 with other years (i.e., 2007 and 2009) used to test the model.

548 Further experimental details are provided in Feng et al. (2011, 2016). Table 1 describes the average,
 549 minimum and maximum values for all measured variables required to run the DO₃SE-Crop model
 550 collected at the Xiaoji site for each year. Additionally, the M7 (mean 7-hour O₃ concentration over
 551 the exposure period in ppb) is included for both AA and E O₃ treatments. Measurements were taken
 552 at a height of 2 metres above the ground surface.

553 Table 1. Summary of hourly meteorological and ozone concentration ([O₃]) data at Xiaoji.

Variable	Unit	Description	Year 2007 (min, avg, max)	Year 2008 (min, avg, max)	Year 2009 (min, avg, max)
PAR_{total}	W/m ²	Direct and diffuse PAR at the top of the canopy	0, 241.94, 1759	0, 265.15, 1810.48	0, 262.16, 1850.5
T_{air}	°C	Surface air temperature in degrees Celsius	-6.35, 10.07, 34.10	-9.22, 8.24, 32.7	-9.17, 9.62, 33.64
VPD	kPa	Leaf to air vapour pressure deficit	0, 0.34, 3.77	0, 0.3, 3.5	0, 0.38, 3.8
u_z	m/s	Wind speed at a reference height z	0.03, 2.14, 8.19	0.07, 2.11, 8.83	0.05, 2.10 8.45
C_z (and M7 value) for AA O ₃ treatment	ppb	Ozone concentration at a reference height z	0, 15.48, 129.95 (47.2)	0, 16.2, 137.07 (49)	0, 15.9, 102.02 (47)
C_z (and M7 value) for E O ₃ treatment	ppb	Ozone concentration at a reference height z	0, 16.83, 176.73 (56.1)	0, 17.46, 171.19 (60.7)	0, 17.95, 153.40 (58.7)
O ₃ exposure period	Days		38	92	92

554

555 2.2 DO₃SE-Crop calibration and evaluation

556 Development and calibration of the DO₃SE-Crop model with the Xiaoji experimental data set
 557 followed three main steps: i). sensitivity analysis to identify key model parameters to calibrate; ii).
 558 calibration of these key parameters for a single year and both tolerant and sensitive cultivars, and
 559 iii). evaluation of key DO₃SE-Crop model outputs for different years and cultivars from those used in
 560 model calibration.

561 To perform the sensitivity analysis we used the SaLIB python library (Iwanga et al., 2022, Herman
 562 and Usher, 2017). The analysis requires ranges to be specified for the parameters (identified by an
 563 initial manual calibration) that are included in the sensitivity analysis. For physiological parameters,
 564 ranges were determined by considering the range of these parameters in the literature. For carbon
 565 allocation parameters, the range was identified by considering the maximum and minimum values of
 566 these parameters that would result in appropriate dry matter partitioning within the plant. Once the
 567 ranges were identified, the sensitivity analysis was run using the extended fourier amplitude
 568 sensitivity analysis, which has been commonly used by other crop modellers to improve their

569 calibrations (Silvestro et al., 2017, Vazquez-Cruz et al., 2014) . From the sensitivity analysis outputs
570 (see Fig S6), the parameters whose variation contributes the most to variations in selected modelling
571 outputs (in this case photosynthetic rate and yield) were identified as the key model outputs for
572 calibration. Using this method we identified the following DO₃SE-Crop parameters as those most
573 important to calibrate: (i) leaf photosynthesis parameters (V_{cmax25} , J_{max25} , kN , m , and VPD_0); (ii) C
574 allocation parameters (α_{root} , α_{leaf} , α_{stem} , Υ , τ) and related dark respiration coefficients (R_{dcoeff}
575 and R_{gcoeff}) which were later included in the calibration after identifying issues with overestimated
576 respiration, likely due to the use of parameter values designed for broad plant functional types,
577 which may not be suitable for wheat). O₃ damage module parameters related to senescence (γ_3 , γ_4 ,
578 γ_5 , and $CLS03$) were not included in the sensitivity analysis, as γ_3 and $CLS03$ is already recognized as
579 important for calibration, and γ_4 and γ_5 were introduced in this study to represent the start (SOS)
580 and end (EOS) of senescence, making both essential for calibration. Phenology parameters were also
581 excluded as earlier studies have shown these are relatively straightforward to calibrate using
582 automated methods for a range of environmental conditions (Nguyen et al., 2024). We note that
583 assessing the probability distribution of these ranges would also be useful but consider this outside
584 the scope of the current paper due largely to data limitations.

585 The DO₃SE-Crop model was then calibrated using the 2008 dataset for the Y2 and Y16 cultivars. The
586 year 2008 was selected since this showed a substantial difference in yield of 208 and 148 g/m²
587 between the AA and EO₃ treatments for the Y2 and Y16 cultivars respectively. These cultivars were
588 chosen since they were identified as the most sensitive (Y2) and tolerant (Y16) cultivars according to
589 the experimental analysis conducted by Feng et al. (2016). See Fig. 5, which shows a diagram
590 representing the calibration process. Calibration of the phenology module used only the Y2 cultivar,
591 AA O₃ treatment data describing the timing of emergence, anthesis and maturity to calibrate key
592 phenology parameters (T_b , T_0 , T_m , VT_{min} , VT_{max} , PIV , and PID , TT_{emr} , TT_{veg} , TT_{rep} , and T_l). The
593 phenology calibration was automated by computationally applying a genetic algorithm (Wang,
594 1997), an optimisation technique with gradient decent to find the best parameters. This uses a
595 combination of crossover strategy (selecting parameters randomly from parameter pairings) and
596 mutation strategy (which takes a parameter range and uses incremental step changes) to identify
597 the parameters which give the highest R², and lowest root mean square error (RMSE) when
598 compared with observations of the timing (day of year) of anthesis and maturity.

599 Calibration of the leaf physiology, canopy C allocation and O₃ damage DO₃SE-Crop modules was
600 performed manually. This required that an initial value and range be defined for each parameter.
601 which were defined from a combination of observations from the Xiaoji experimental dataset as well
602 as values taken from the literature (see Table A1 and A2 of the Appendix A for details). The model
603 was manually calibrated until certain conditions were satisfied, as explained below. Calibration of the
604 leaf physiology parameters (V_{cmax} , J_{max} , kN , m , and VPD_0) was performed only the Y2 cultivar, AA
605 O₃ treatment whilst keeping all other parameters fixed. This calibration aimed to achieve a
606 maximum A_{net} value of 30 $\mu\text{mol CO}_2 \text{ m}^{-2} \text{ s}^{-1}$ and a g_{O_3} value of 350 $\text{mmol O}_3 \text{ m}^{-2} \text{ PLA s}^{-1}$, consistent
607 with the maximum values observed in the Xiaoji dataset (Zhu et al., 2011). We calibrated V_{cmax} and
608 J_{max} as measurements are only provided for Y2 and Y16 cultivars and only for certain points during
609 the growth period and we know that V_{cmax} and J_{max} can vary seasonally.

610 Calibration of the C allocation parameters (α_{root} , α_{leaf} , α_{stem} , Υ , τ and related dark respiration
611 coefficients (R_{dcoeff} and R_{gcoeff}), was also performed keeping all other parameters fixed. This
612 calibration aimed to achieve the following criteria:- a stem dry matter to leaf dry matter ratio (R_{SL})
613 of approximately 2:1 (Huang et al., 2022); relative growth of different plant parts (i.e. leaves, stem,
614 roots, grain) consistent with profiles found in the literature (Osborne et al., 2015; de Vries et al.,
615 1989); a modelled *Grain DM* within $\pm 30\%$ of the observed; an *above ground DM* value of
616 between 1200-1600 g m^{-2} ; an *LAI* value between 4-7 $\text{m}^2 \text{ m}^{-2}$; and an R_d value of between 30 to 60%
617 of A_{net} (Amthor et al., 2019). We calibrated C allocation parameters as in the JULES-crop model

618 calibration has only been performed for broad, global scale application for wheat (Osborne et al.,
619 2016) and therefore requires further calibration for application under Chinese conditions. Further,
620 the observed dataset does not provide any information with regards to the change in carbon
621 allocation parameters due to ozone. The C allocation parameters were only calibrated for ambient
622 ozone conditions, and we only investigate the effect of ozone on C assimilation (not C allocation).

623 Finally, calibration of the O₃ parameters (γ_3 , γ_4 and γ_5) was performed using 2008 data for both the
624 Y2 and Y16 cultivars whilst again keeping the other parameters fixed. Calibration was targeted so
625 that the difference in *Grain DM* between ambient and elevated O₃ treatments as close as possible
626 to $\pm 10\%$ of the observed.

627 The manual calibration process consisted of three stages as explained above, as well as comparisons
628 with established information on wheat growth from the literature. By reducing the number of
629 parameters involved in the calibration, the chance of equifinality (multiple combinations of
630 parameters yielding similar results) was minimised (Beven, 2006). The parameters identified by the
631 sensitivity analysis were varied within realistic ranges to obtain a parameterization that closely
632 approximates wheat physiological processes. Multiple parameterizations were tested to avoid
633 convergence on local minima in R² and RMSE. While further fine-tuning of the parameter ranges
634 could potentially improve yield prediction, it might also disrupt simulations of other key plant
635 processes, such as carbon allocation or photosynthesis. The calibration approach balances the need
636 for accurate output simulation with the physiological realism required for wheat growth under the
637 conditions of this study. Though it is difficult to claim that the absolute optimal parameter set has
638 been achieved, this limitation is common to any model calibration (Wallach, 2011). The current
639 parameterisation represents a physiologically realistic simulation of wheat growth under the
640 conditions of the present study using a robust calibration method.

641 Evaluation of the DO₃SE-Crop model was conducted using Xiaoji data for 2007 and 2009 for all
642 cultivars, and 2008 data for Y19 and Y16 cultivars. This evaluation tested the ability of the calibrated
643 DO₃SE-Crop model to simulate *Grain DM* using R² and RMSE statistical tests.

644

645

646 Results

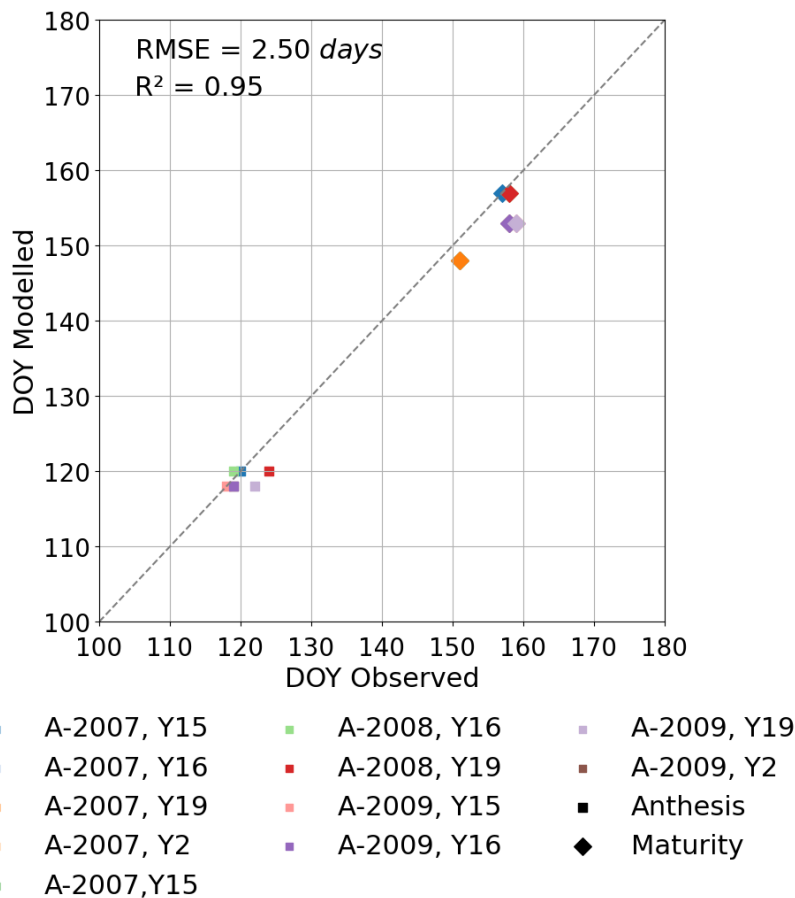
647 We first examine the model's ability to simulate the key phenological development stages since this
648 is key to simulating the variation in C allocation to different plant parts over the course of the
649 growing season and hence how O₃ exposure will influence growth and yield which is determined by
650 the timing and length of the grain filling period. We also explore how DO₃SE-Crop simulates within
651 canopy [O₃] profiles to understand which layers of the canopy are most important in determining O₃
652 response. We then examine the ability of the model to simulate leaf-level physiology and C
653 allocation to the different parts of the crop. Lastly, the impact of both instantaneous and long-term
654 O₃ damage on the crop's final *Grain DM* is evaluated for different cultivars and years.

655 i) Crop Phenology

656 The Xiaoji dataset provides sowing and harvest dates for all cultivars for each year but only provides
657 the date of the timing of anthesis for the years 2008 and 2009 for all cultivars. We assume that DVI =
658 1 is equivalent to the start of anthesis and that this occurs 4-5 days after flag leaf emergence as
659 shown in Fig. 2. We determine the influence of O₃ on the start and end of senescence (SOS and EOS)
660 using the breakpoint method (described in Pande et al., 2024) to assess significant changes in the
661 chlorophyll values that indicate senescence onset and rate of change for the quantification of tl_{ep}
662 and tl_{se} . This method is applied for chlorophyll data collected in 2008 under both AA and E O₃
663 treatments for the Y2 cultivar. We then assume that these key phenology parameters (i.e., TT_{emr} ,
664 TT_{veg} , TT_{rep} , tl_{ep} and tl_{se}) are consistent across cultivars and years. Our results in Fig 3 suggests
665 this is a reasonable assumption however, we appreciate that assuming these phenology parameters
666 will work for a wider variety of cultivar types (e.g., early or late sown and/or maturing) and years
667 with rather different meteorological conditions, needs to be done with caution.

668 Fig S1 shows the modelled vs observed timing of anthesis and harvest for the training dataset. Fig 3
669 shows the same for the test dataset. For the test dataset there is a variation of 2 to 4 days and 1 to 6
670 days for the modelled anthesis and maturity in relation to observed anthesis and maturity
671 respectively, with observed phenology tending to be a little later than modelled. The T_l ranges
672 between 1325 and 1478 °C days for the three years, with crop sowing occurring between 315 and
673 324 days of year and harvests occurring between 135 and 151 day of year (of the following year).
674 The number of days from the modelled crop sowing to harvest was between 181 and 191 for the
675 three years, compared to 198 and 201 for the observations.

676 Fig. 3 Modelled vs observed phenological stages provided as day of year (DOY) for the test dataset
 677 (i.e., excluding the year 2008 for the Y2 cultivar).

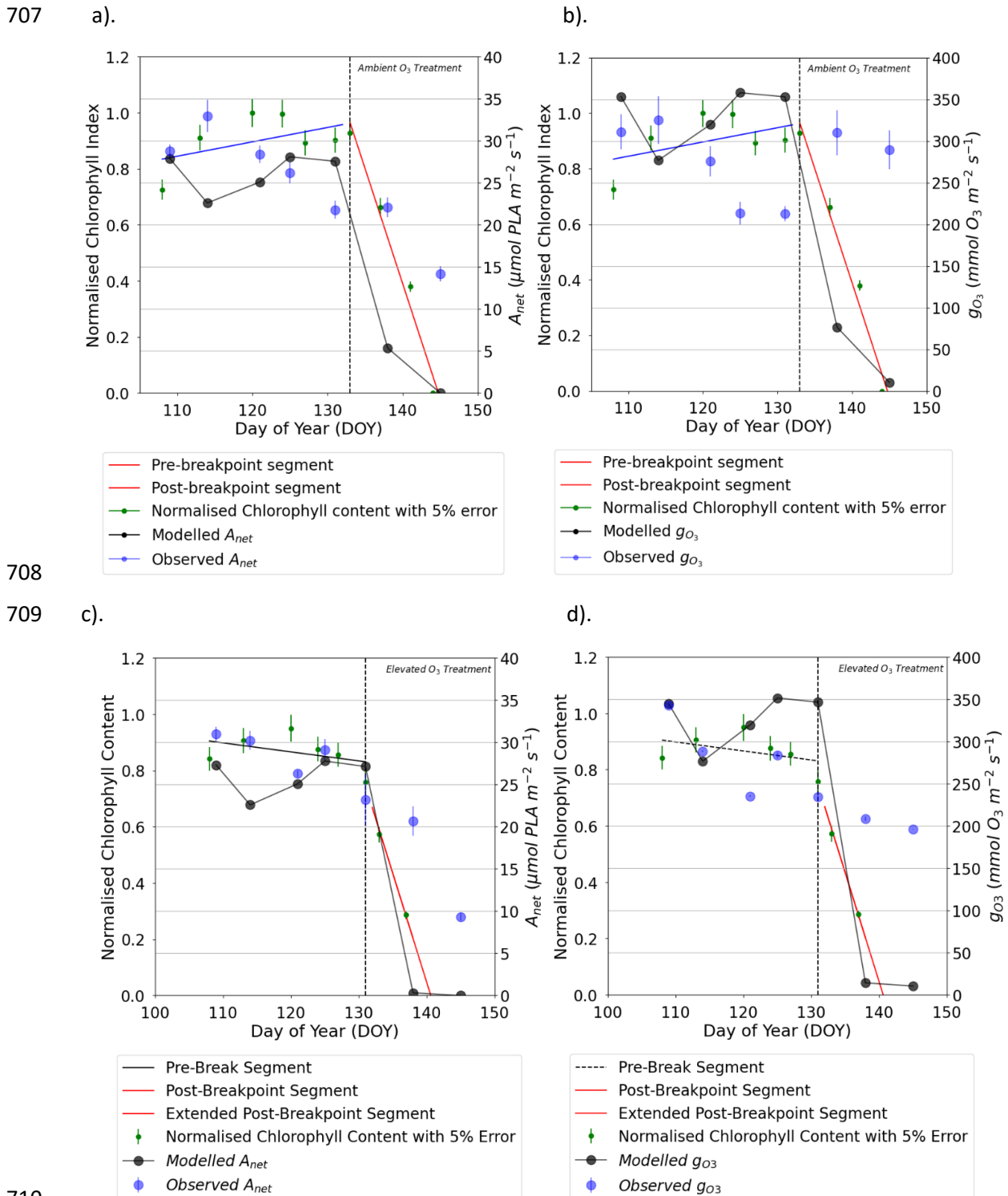


678

679 ii). Leaf physiology variables (A_{net} , g_{O_3})

680 The DO₃SE-Crop model was able to simulate the seasonal A_{net} and g_{O_3} with values ranging from 0 to
 681 27 $\mu\text{mol CO}_2 \text{ m}^{-2} \text{ s}^{-1}$ and 10 to 351 $\text{mmol O}_3 \text{ m}^{-2} \text{ s}^{-1}$ for A_{net} and g_{O_3} respectively over the course of
 682 the growing season (see Fig 4). The simulated daily maximum values of modelled g_{O_3} , at 351 $\text{mmol O}_3 \text{ m}^{-2} \text{ s}^{-1}$,
 683 were within the range of the observed value of 340 $\text{mmol O}_3 \text{ m}^{-2} \text{ s}^{-1}$. Similarly, the
 684 modelled daily maximum A_{net} is 27 $\mu\text{mol CO}_2 \text{ m}^{-2} \text{ s}^{-1}$ compared to observed value of 28 $\mu\text{mol CO}_2 \text{ m}^{-2}$
 685 s^{-1} for the period between anthesis and 10 days before maturity for the year 2008, for the Y16
 686 cultivar (similar results were obtained for the Y2 cultivar; see Fig. S5). In Fig. 4a and b, the steep
 687 decline in modelled A_{net} and g_{O_3} is not seen in the observed dataset. This discrepancy may occur
 688 since the simulated A_{net} and g_{O_3} values represent sunlit parts of the upper canopy which comprise
 689 both green and senesced leaf material. In contrast, observed A_{net} and g_{O_3} values are measured
 690 specifically on the flag leaf and most likely only for the green parts of the leaf, since the LI-6400
 691 photosynthesis system mounted with a 6400–40 leaf chamber fluorometer (used to measure A_{net}
 692 and g_{O_3} in the Xiaoji experiment, Feng et al., 2016) will not provide values for senesced leaf
 693 material. See also Figure 4 which combines A_{net} and g_{O_3} with observed normalised chlorophyll
 694 content and clearly shows the leaf is senescing as predicted by the model. However, the decline in
 695 observed chlorophyll values aligns well with the decline in modelled A_{net} and g_{O_3} with the timing of
 696 the earlier onset of senescence by 0-3 days between the AA and E O₃ treatments being captured well
 697 by the model. It is useful to note that the calibrated V_{cmax} and J_{max} values match the observed
 698 values within $\pm 2 \mu\text{mol CO}_2/\text{m}^2/\text{s}$.

699 Fig 4. Comparison of daily maxima seasonal profiles of DO₃SE-Crop modelled canopy leaf vs observed
 700 flag leaf data for a). AA O₃ treatment A_{net} , and b). AA O₃ treatment g_{O_3} and c) E O₃ treatment A_{net} ,
 701 and d). E O₃ treatment g_{O_3} for the period from the anthesis (i.e., TT_{rep}) for the year 2008 and the
 702 Y16 cultivar. The left (solid blue line) and right (solid red line) represent the segment fits to the
 703 normalised chlorophyll content values for application of the breakpoint method to define the SOS
 704 (Start of Senescence) shown as the solid black dashed line. The green scatter solid dots, along with
 705 their standard measurement error, represent the normalised observed chlorophyll content values
 706 (see Fig 7 for further details).

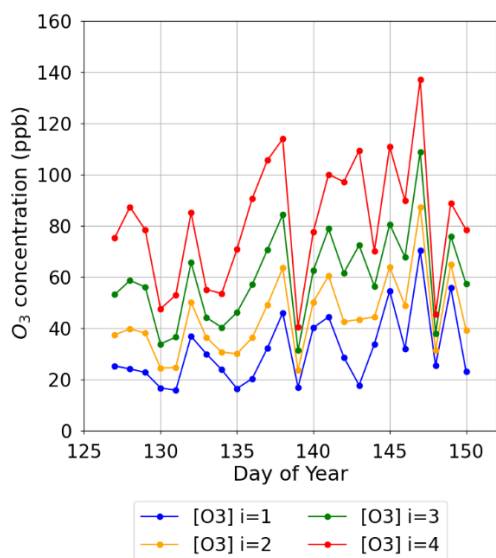


712 iii). Within canopy variation in O₃ and physiology

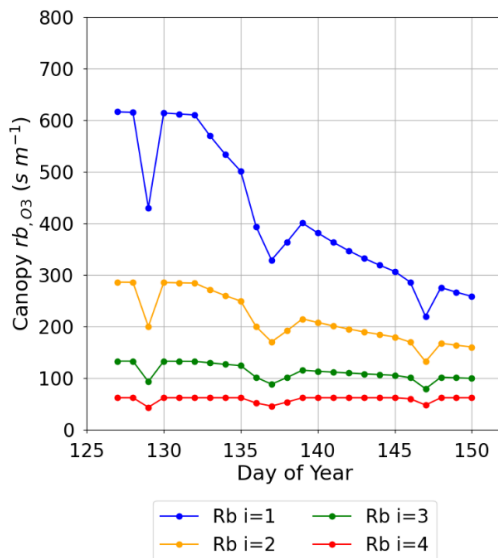
713 An important determinant of O₃ deposition and damage is stomatal O₃ deposition (our $gO3_c$) which
 714 is a function of within canopy transfer of O₃ and stomatal and non-stomatal deposition. The multi-
 715 layer aspect of the DO₃SE-Crop model allows within canopy stomatal and non-stomatal O₃
 716 deposition to be simulated. Fig 5 shows the variation in key variables that determine total and
 717 stomatal O₃ canopy deposition across 4 canopy layers as a mid-day average over the course of the
 718 tl_{ep} period of the flag leaf, for the year 2008 and the Y16 cultivar.

719 Fig 5. Plot showing variation in key O₃ deposition terms as daily maxima by canopy layer (N.B. $i = 4$
 720 is the top canopy layer, $n = 4$) a). O₃ concentration at the top of each layer, b). leaf boundary layer
 721 resistance by canopy layer (rb_{O3}), c). PAR for the sunlit LAI component of each layer (PAR_{sun}) and
 722 d). leaf level stomatal conductance to O₃ (g_{O3}) for the period from anthesis (i.e., TT_{rep}) for the Y16
 723 cultivar and for the E O₃ treatment in 2008.

724 a).

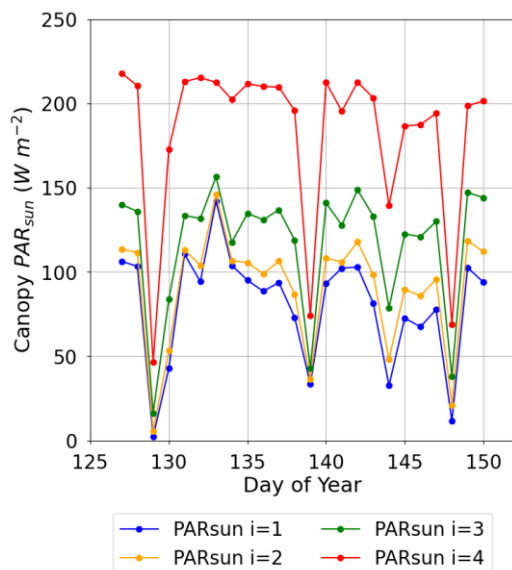


b).

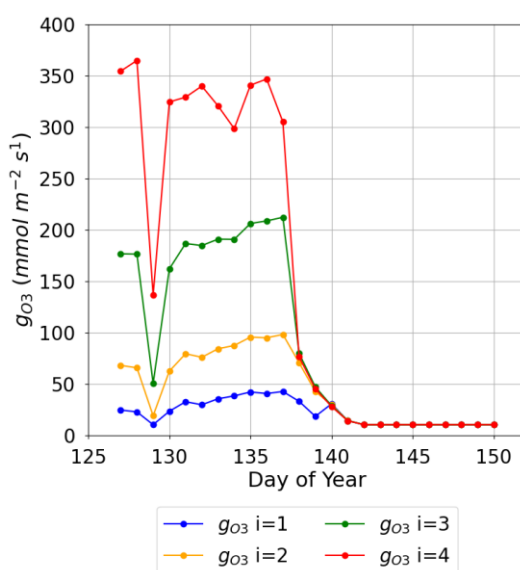


725

726 c).



d).



727

728

729 Figure 5a. shows a decrease of within canopy O_3 concentration from highs of around 140 ppb to
730 values within the range of 10 to 50 ppb between the top of the canopy and bottom canopy layer, the
731 penetration of O_3 into the canopy increases over time as the canopy senescence and O_3 uptake is
732 reduced. Similarly, PAR_{sun} reduces from maximum values of around 200 W m^{-2} at the top of the
733 canopy to values of around 100 W m^{-2} in the lower canopy layers even on sunny days (see Fig. 5c).
734 The leaf rb_{O_3} (Fig. 5b) increases with canopy depth with resistances in the region of approximately
735 50 s m^{-1} at the top of the canopy to values of around 600 s m^{-1} at the bottom of the canopy, this will
736 limit stomatal O_3 uptake in the lower canopy layers, finally these factors combine to influence
737 canopy level g_{O_3} (Fig. 5d) which reduces from values of around 350 at the top of the canopy to 20
738 $\text{nmol } O_3 \text{ m}^{-2} \text{ s}^{-1}$ at the bottom of the canopy layer, these differences in leaf rb_{O_3} and g_{O_3} reduce with
739 the onset of senescence. This analysis shows the importance of interplay between these different
740 factors for an accurate whole canopy estimate of O_3 deposition.

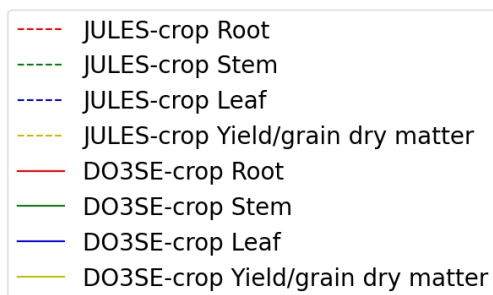
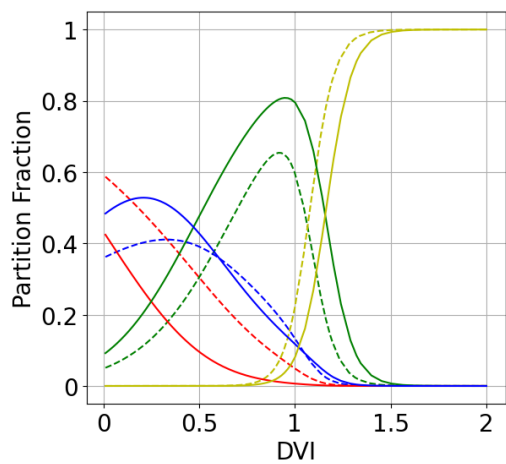
741 iv) Crop development, biomass and yield.

742 The dry matter dynamics of the different parts of the crop are shown in Fig. 6. The modelled
743 *Grain DM* value of 851 g m^{-2} was reasonably close to the observed value of 888 g m^{-2} . The stem to
744 leaf dry matter ration (R_{SL}) is 2.1:1 and therefore in the range provided in the literature (Huang et
745 *al.*, 2022). The above-ground biomass values of 1510 g m^{-2} also match reasonably well against the
746 1200 to 1600 g m^{-2} range described in the literature (Huang et al., 2022; Liu et al., 2022). Further, the
747 partition fraction profiles are consistent with those of Osborne *et al.* (2015) as shown in Fig. 6a) with
748 the main differences being that the modelled stem and root partition profiles are somewhat higher
749 and lower, respectively. The JULES model comparison is provided for illustrative purposes only (i.e.
750 this model has not been calibrated with the Xiaoji data but rather is a parameterisation suggested
751 for global application).

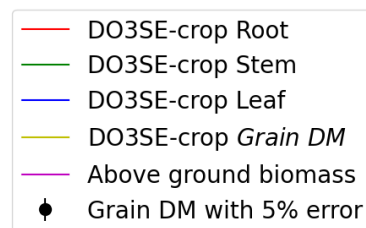
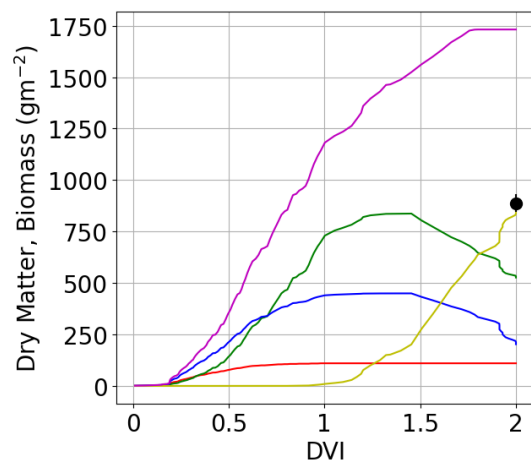
752 Fig 6. Seasonal profiles (i.e., plotted against *DVI*) of carbon allocation variables for the Xiaoji
753 calibrated DO_3 SE-Crop model (i.e. AA O_3 treatment, year 2008 and Y16 cultivar) with a). showing the
754 partition fractions of the daily accumulated *NPP* partitioned to roots, stems, leaves, and grains for
755 the Xiaoji calibrated DO_3 SE-Crop model (solid lines) vs the JULES Crop model (dashed line) calibrated
756 for global application after Osborne *et al.* (2015)) and b). showing the *DM* (in g/m^2) of daily
757 accumulated *NPP* partitioned to roots, stems, leaves, and grains with the observed final *GrainDM*
758 for Y16 cultivar in 2008 also shown (solid black dot with 5% error).

759

760 a).



b).



761

762 v). O₃ induced yield loss difference between tolerant and sensitive cultivars: Instantaneous and long-
763 term senescence impact.

764 The *Grain DM* is assumed to be damaged by both the instantaneous impact of O₃ (Farage et al.,
765 1991) on photosynthesis as well as a longer-term O₃ effect that can lead to enhanced senescence
766 (Feng et al., 2022). To explore which of these damage mechanisms is most important we calculated
767 the difference in the *Grain DM* caused by carbon assimilation for the AA and E O₃ treatments as
768 compared to a simulated very low O₃ treatment representing pre-industrial conditions (for which C_z
769 O₃ concentration did not exceed 15 ppb) for both the tolerant (Y16) and sensitive (Y2) cultivar for
770 each of the three years (see Table 2). We found a negligible effect of O₃ (0 to 0.2 %) on *Grain DM*
771 due to the instantaneous effect of O₃ on photosynthesis, which could perhaps be partly due to the
772 the crops ability to recover photosynthetic capacity overnight, compared to a highly significant (9.85
773 to 31.13 %) impact due to the long-term O₃ effect on carbon assimilation *via* the enhancement of
774 senescence on final *Grain DM*. Table S3 shows the observed % *Grain DM* loss compared to a
775 modelled pre-industrial O₃ scenario due to the combination of instantaneous and long-term ozone
776 effect.

777

778 Table 2. Simulations of % *Grain DM* loss that compare ambient (AA) and elevated (E O₃) treatments
 779 with a pre-industrial O₃ scenario divided between *Grain DM* losses caused by the instantaneous
 780 effect O₃ on photosynthesis and the long-term O₃ effect on senescence. The effect of both damage
 781 O₃ mechanisms acting together are also shown.

Year	Tolerant: Instantaneous O ₃ effect on % <i>Grain DM</i>		Tolerant: Long-term O ₃ effect on % <i>Grain DM</i>	
	Ambient versus pre-industrial	Elevated versus pre-industrial	Ambient versus pre-industrial	Elevated versus pre-industrial
2007	0	0.2	16.60	29.05
2008	0	0	9.85	24.37
2009	0.03	0.03	17.48	25.87
	Sensitive: Instantaneous O ₃ effect on % <i>Grain DM</i>		Sensitive: Long-term O ₃ effect on % <i>Grain DM</i>	
	Ambient versus pre-industrial	Elevated versus pre-industrial	Ambient versus pre-industrial	Elevated versus pre-industrial
2007	0	0.01	18.43	31.13
2008	0	0	13.43	29.14
2009	0.01	0.01	19.5	28.11

782

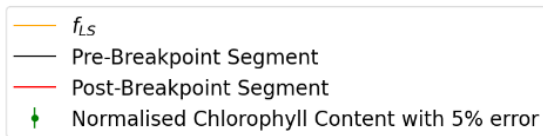
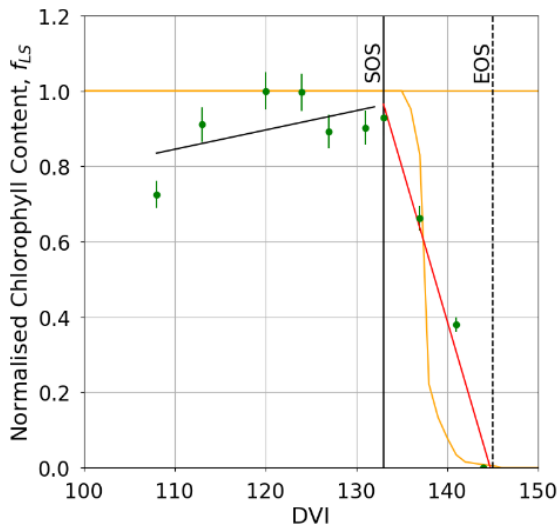
783 vi). Senescence

784 The breakpoint method (Mariën et al., 2019) was used to determine the onset (SOS) and end (EOS)
 785 of senescence and maturity respectively using the chlorophyll data which was available for the year
 786 2008, and the Y16 and Y2 cultivars. Results in Fig. 7 and Fig. S4 show that the E-O₃ treatment for
 787 cultivars Y16 and Y2 brought forwards the SOS by 3 and 5 days (see Fig. 7) respectively, and EOS by 6
 788 and 9 days (see Fig. S4) respectively. Fig 7 also shows the f_{LS} profile which denotes the DO₃SE-Crop
 789 models accumulated stomatal O₃ flux effect on senescence, it is clear that f_{LS} is able to simulate the
 790 change in normalised chlorophyll content reasonably well. The slope of the ambient f_{LS} is already
 791 steep since the ambient treatment already has rather high O₃ levels as is now made clear in Table 1
 792 with a value of 47ppb. According to the M7 wheat dose-response relationship this would result in a
 793 yield loss of ~ 5%.

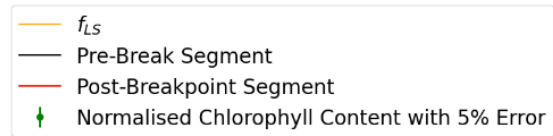
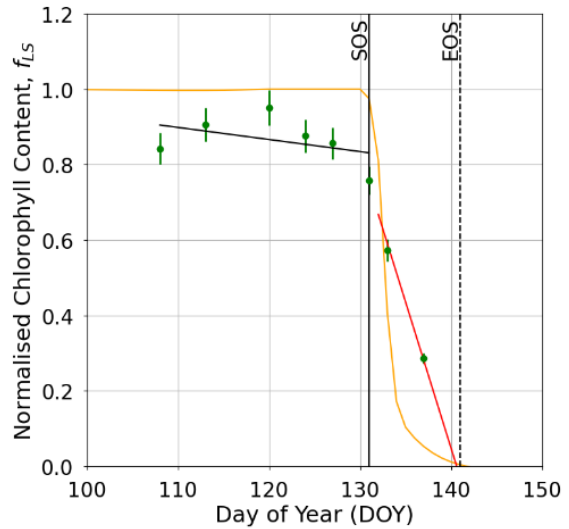
794 Fig 7. Profiles of O₃ induced leaf senescence for the Y16 cultivar for the a). AA O₃ treatment and b). E
 795 O₃ treatment. The timing of the SOS (solid black line) and EOS (dashed black line) were determined
 796 by applying the break point method to the chlorophyll data and are shown in relation to the f_{LS}
 797 simulations of senescence (yellow solid line). The observed normalised chlorophyll content data,
 798 shown as filled blue symbols, include error bars representing the standard deviation of the
 799 measurements.

800

801 a).



801 b).



802

803 vii). *Grain DM* simulations across years and between cultivars

804 Fig. 8 shows a box plot of the modelled vs observed *Grain DM* for both the sensitive (Y2, Y19) and
805 tolerant (Y15, Y16) cultivars for each O₃ treatment (AA and E) for the years 2007, 2008 and 2009 (i.e.
806 all data). Given the variability in the experimental data the model simulates the difference in
807 *Grain DM* between the AA and E O₃ treatments reasonably well with a simulated reduction in
808 *Grain DM* of 29 to 131 g m⁻² compared with observed values of 81 to 165 g m⁻² for the tolerant;
809 and 49 to 196 g m⁻² compared with observed values of 54 to 293 g m⁻² for the sensitive cultivars
810 respectively. The most notable difference is that there is a larger range in the simulated
811 *Grain DM* losses of the modelled sensitive cultivars though the simulated mean value for absolute
812 *Grain DM* suggests a more conservative influence of O₃ with yields at 610 g m⁻² vs observed average
813 yields of 590 g m⁻².

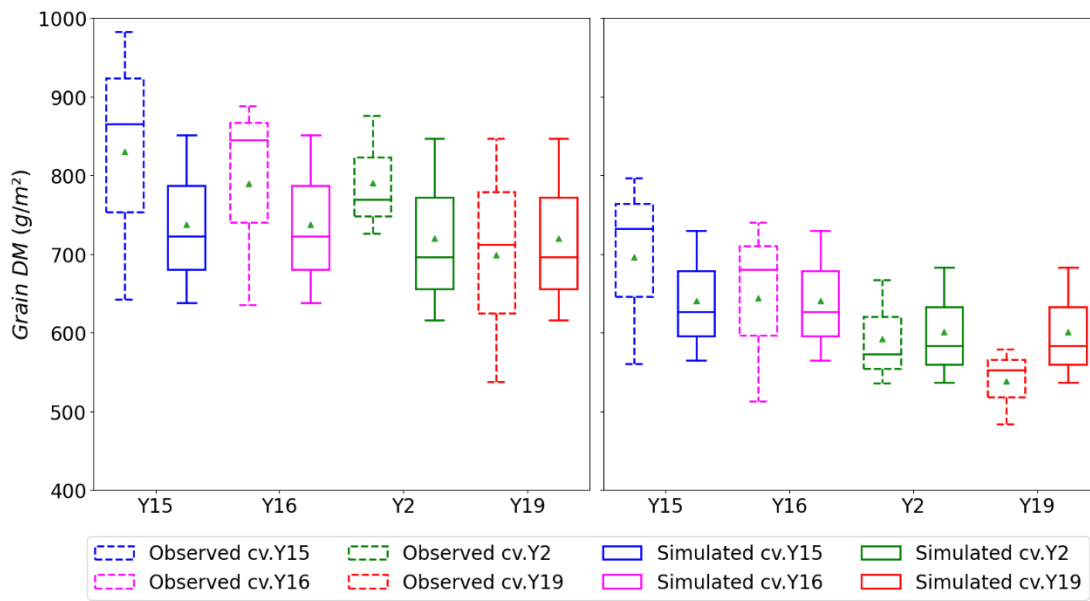
814

815 Fig 8. Boxplots (crosses: 0.01 and 0.99 percentiles; box: 0.25 quartile, median and 0.75 quartile;
816 triangle: mean) of simulated and observed wheat *Grain DM* for the tolerant (Y15 and Y16) and
817 sensitive (Y2 and Y19) cultivars under a.) AA and b.) E O₃ treatment for the years 2007, 2008 and
818 2009; these data include all the dataset.

819

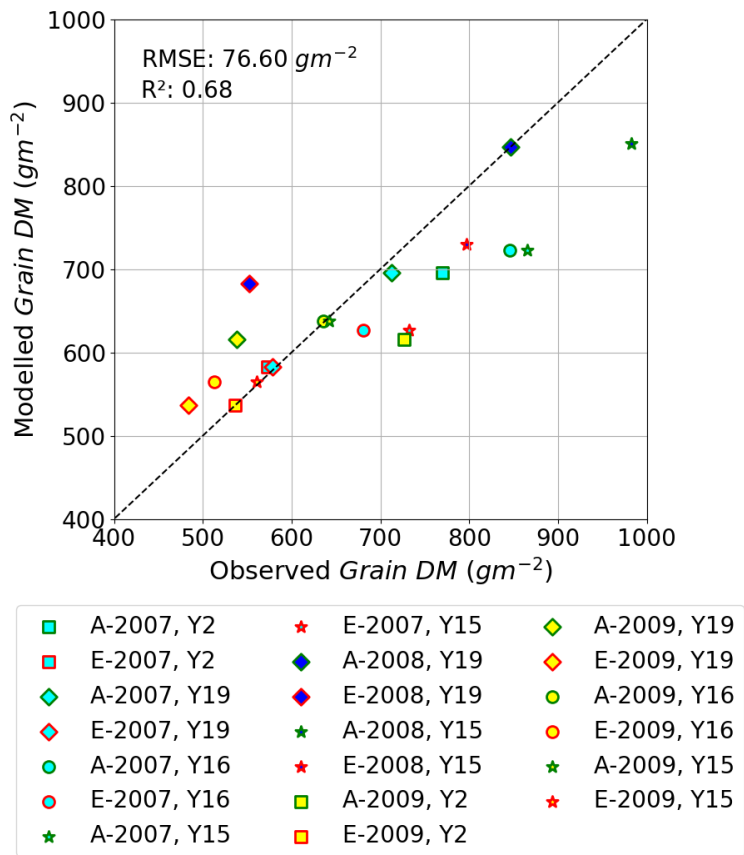
820 a).

b).



822 Finally, Fig 9 shows the relationship between modelled vs observed *Grain DM* (in g m^{-2}) as a scatter
823 plot, a linear regression through these data gives an R^2 value of 0.68 and RMSE of 76 g m^{-2} , showing
824 the model is able to simulate with reasonable accuracy the differences in absolute yield for different
825 cultivars and for different years. There are some instances of both underestimation and
826 overestimation, however the deviations from the 1:1 line is not excessively large. These model test
827 results compare with an R^2 of 0.92 ($n=4$) and an RMSE of 25.49 g m^{-2} for the training dataset (Y2 and
828 Y16 cultivar and year 2008, see Figure S3), the stronger agreement between observed and modelled
829 training dataset, as well as the reasonable agreement for the entire dataset would suggest the
830 model is not over-fitted. We find that we tend to underestimate the O_3 -induced relative yield loss
831 (RYL) by between -2.76 and 15.34 (observed less modelled RYL) across all years and cultivars.

832 Fig. 9. A scatter plot showing modelled vs observed *Grain DM* (in $g\ m^{-2}$) for the AA and E O₃
 833 treatments for all 4 cultivars and 3 years of the Xiaoji dataset; these data include those used for
 834 evaluation.



835

836 Discussion

837 The DO₃SE-Crop model was found capable of simulating O₃ damage to grain yield for O₃-FACE
838 conditions at the experimental site in Xiaoji, China with a good degree of accuracy. Simulated
839 relative yield losses (RYLs) between AA and E O₃ treatments for all years ranged between 11 to 14%
840 and 13 to 19% for tolerant and sensitive cultivars respectively, these tend to be lower (particularly
841 for the more extreme O₃ induced yield losses of the sensitive cultivars) than the observed values of
842 13 to 20% and 10 to 35%. Overall, simulations of tolerant and sensitive cultivars underestimated
843 RYLs by 4% and 7% respectively on average across years and cultivars (see data in section S6). This
844 would suggest that O₃-induced yield losses can be more reliably modelled for tolerant cultivars,
845 possibly because additional processes causing O₃-induced yield losses in sensitive cultivars are not
846 captured. Such processes might include the effect of O₃ on the allocation of carbon to different plant
847 parts (Feng et al., 2008) or O₃ inducing additional respiratory costs *via* the upregulation of defence
848 mechanisms (Biswas et al., 2008). The model was also able to simulate absolute
849 *Grain DM* reasonably well. Under AA O₃ levels *Grain DM* simulated for all years and cultivars were
850 between 616 and 851 g/m² compared to observations of between 537 and 982 g/m². There is a
851 tendency to overestimate *Grain DM* under ambient conditions and underestimate *Grain DM* under
852 elevated O₃ which is reflected in the RYL values.

853 Overall, the DO₃SE-Crop model simulation results compare favourably to results made by the
854 MCWLA-Wheat model (Tao et al., 2017) which was also calibrated for the Xiaoji experimental
855 conditions but without distinction between tolerant and sensitive varieties. MCWLA-Wheat
856 simulations of absolute yield varied between ~5700 and 9000 kg/ha (compared to ~5700 to 9800
857 kg/ha) for ambient and ~4800 to 8000 kg/ha (compared to ~5200 to 8000 kg/ha) for elevated O₃
858 treatments. A mean relative yield loss of 14% was simulated by the model.

859 It is useful to set these site-specific estimates of O₃-induced yield losses in the context of yield losses
860 estimated using more traditional, concentration based O₃ risk assessment methods. A seminal paper
861 by Feng et al. (2022) estimated mean relative yield losses across East Asia due to ambient O₃
862 concentrations at 33% (with a mean range of 28 to 37%) according to a mean monitored O₃
863 concentrations of 30.9 ppm h expressed as AOT40 (six-month accumulated daytime O₃
864 concentration above a threshold of 40 ppb). The mean difference in AOT40 (accumulated over only
865 75 days) between the AA and E O₃ treatments at Xiaoji across all years was 7.8 ppm h giving a mean
866 relative yield loss of approximately 10 to 20% depending on year and cultivar. As such, our modelled
867 results in terms of RYLs between AA and E O₃ treatments are consistent with these broader results
868 for East Asia.

869 Crop phenology plays a crucial role in determining the timing of the important O₃ exposure period
870 (i.e., from anthesis to maturity), and hence O₃ damage. Evaluation of the DO₃SE-Crop phenology
871 model shows the model is able to accurately simulate crop phenology for the three years at Xiaoji (R²
872 =0.95 and RMSE =2.5, see Fig. 3). Estimating the correct timing of anthesis is crucial since the period
873 from anthesis to crop maturity is the O₃-sensitive period. During this period, accumulated stomatal
874 O₃ flux (acc_{fst}) will contribute to early and enhanced senescence once the critical threshold
875 ($CLsO3$) is exceeded. This period also coincides with carbon accumulation in the grain (Kohut et al.,
876 1987; Feng et al., 2008) which may be limited by O₃-induced early onset or enhanced senescence.
877 The DO₃SE-Crop model was developed to accommodate the full range of effects of O₃ on senescence
878 with revised functions, similar to those first developed by Ewert and Porter (2000), able to modify
879 both the O₃ induced onset of senescence as well as the O₃ effect on maturity. This is important since
880 experimental evidence has shown that O₃ can bring forward the maturity date; for example, the flag

881 leaf was found to have senesced 25 days earlier in a high O₃ treatment, compared to a charcoal-
882 filtered treatment (Grandjean and Fuhrer, 1989; Gelang et al., 2000). O₃ was also found to cause
883 differences in the time to maturity of the flag leaf, with Shi et al. (2009) reporting that maturity was
884 brought forward by 8 days under an elevated O₃ treatment (50% higher than ambient). Currently,
885 other crop models with O₃ damage functions (e.g. MLCWLA-Wheat (Tao et al., 2017) and LINTULLCC-
886 2 (Feng et al., 2022) are only able to bring the O₃-induced onset of senescence earlier.

887 The DO₃SE-Crop model is also able to simulate differential O₃ uptake in each canopy layer. Fig. 5
888 shows that the majority of stomatal O₃ uptake occurs in the sunlit layers of the upper canopy. Similar
889 results were found in an experimental study on a productive grassland in Switzerland (Jaggi et al.,
890 2006) who found that different levels of O₃ exposure to canopy components predominantly located
891 in the upper and lower parts of the canopy support a multi-layer approach to modelling O₃ uptake.
892 Therefore, the focus on the upper canopy by flux-based O₃ metrics (e.g. the phytotoxic ozone dose
893 POD_y , (UNECE, 2017) seems rational in the absence of multi-layer modelling. Crop models such as
894 LINTULCC-2 (Feng et al., 2022) also focus on estimating stomatal O₃ uptake at the top of the canopy
895 to estimate O₃ induced yield losses. For wheat, such an approach is further supported by the fact
896 that the upper canopy layers consist of the flag leaf, which plays a crucial role in photosynthesis and
897 grain filling (Pleijel et al., 2007). The multi-layer functionality of the DO₃SE-Crop model may however
898 become more useful when considering crops that partition assimilated carbon to harvest organs
899 earlier in their growing season such as potato (Okrah et al. 2023).

900 Our results show that the DO₃SE-Crop model was able to estimate the seasonal course of leaf A_{net}
901 and g_{O_3} daily maxima observed at the Xiaoji site (see Fig. 4a) and when compared to other literature
902 describing leaf physiological variables (Guan et al., 2015; Li et al., 2022). This suggests the coupled
903 $A_{net}g_{sto}$ model is working for Chinese conditions (having previously been applied and evaluated for
904 European O₃ experimental conditions – see Pande et al., 2024). The leaf physiology parameters used
905 in this study (i.e. for Asian conditions and cultivars) are higher than parameters for European studies.
906 For Europe, V_{cmax} values of between 60 and 90 $\mu\text{mol CO}_2 \text{ m}^{-2} \text{ s}^{-1}$ were found in the literature (Feng
907 et al., 2022; Pande et.al., 2024, Van Oijen and Ewert, 1999) compared to the observed mean
908 maximum value of 137 $\mu\text{mol CO}_2 \text{ m}^{-2} \text{ s}^{-1}$ at Xiaoji which was used in this study. Similarly, European
909 J_{max} values ranged from 160 to 180 $\mu\text{mol CO}_2 \text{ m}^{-2} \text{ s}^{-1}$ (Feng et al., 2021, Pande et al. 2024, Van Oijen
910 & Ewert, 1999) compared to the observed Xiaoji mean maximum value of 228 $\mu\text{mol CO}_2 \text{ m}^{-2} \text{ s}^{-1}$. Even
911 though these leaf physiology parameters are higher, absolute yields for these Chinese cultivars are
912 consistent with those found under European conditions. This most likely reflects the importance of
913 other environmental conditions (e.g., high vapour pressure deficits) limiting leaf carbon assimilation.
914 Moreover, the complex interactions between O₃ exposure and the plants' physiological responses
915 also play a crucial role. Ozone significantly affected antioxidative enzymes, thereby limiting overall
916 photosynthetic efficiency and yield, particularly in O₃-sensitive cultivars, despite their ability to
917 maintain high carboxylation capacity.

918 Ensuring the seasonal variation in carbon allocation to the different components of the crop (i.e.,
919 roots, stem, leaves and harvest organs) is essential for the simulation of crop growth and yield.
920 There are limited data in the literature that provide these variables, so we compare our results to
921 the carbon allocation profiles described for wheat provided in the original JULES Crop model
922 description, recognising this is intended for wheat grown globally. The DO₃SE-Crop model carbon
923 allocation to the stem and roots is comparatively higher than was simulated by JULES Crop (Osborne
924 et al., 2015; see Fig. 6a). However, we can justify the carbon allocation coefficients used for Xiaoji
925 since the DO₃SE-Crop model was able to distribute carbon to different plant components to produce
926 a well-proportioned plant over the course of the growing season, this was determined by the
927 calibration to a number of key crop variables (i.e., ratios of plant respiration, LAI , stem to leaf dry

928 matter, above ground components and grain dry matter). Importantly, when applied to the test
929 dataset (i.e. excluding 2008 data for the Y2 and Y16 cultivar), the model, was found to simulate the
930 grain dry matter under ambient and elevated O₃ treatments to within 7.9-8.7% of the observed
931 values (R² =0.68, 76 g/m² see Fig. 9).

932 The DO₃SE-Crop model, similar to other crop models with O₃ damage functions (i.e. MLCWLA-Wheat
933 (Tao *et al.*, 2017) and LINTULLCC-2 (Feng *et al.*, 2022), WOFOST (Nguyen *et al.*, 2024)) has the
934 capacity to simulate both the instantaneous and long-term O₃ impact on wheat grain yield. The
935 instantaneous O₃ effect on photosynthesis may cause leaf cell damage and decrease the supply of
936 carbohydrate precursors which can significantly decrease g_{O_3} , V_{cmax} and leaf chlorophyll content
937 (Farage *et al.*, 1991). Elevated O₃ also leads to generation of reactive oxygen species (ROS) in plant
938 cells which can cause oxidative damage to various cellular components. Rubisco, the enzyme
939 responsible for carbon fixation in the photosynthetic process, can be particularly susceptible to this
940 damage, leading to a reduced carboxylation rate (V_{cmax}). Such an O₃ effect on V_{cmax} reduces net
941 photosynthesis and can also induce early senescence shortening the grain filling period (Triboi and
942 Triboi-Blondel, 2002).

943 Results from the DO₃SE-Crop model found a larger impact on yield due to the long-term O₃ impact
944 causing relative yield loss of between 10 to 31% compared to only 0 to 0.2% resulting from the
945 instantaneous O₃ impact on photosynthesis. Previous studies have also found that the long-term O₃
946 effect has a larger impact on yield compared to the instantaneous effect of O₃ on photosynthesis
947 (Emberson *et al.*, 2018; Brewster *et al.*, 2024). Senescence is an age-dependent process of
948 degradation and degeneration that allows nutrients to be re-distributed to different plant organs
949 (Lim *et al.*, 2007). Under O₃ stress, this process is often found to occur earlier and more rapidly in
950 leaves as well as at the whole plant or crop canopy scale (Brewster *et al.*, 2024). The causes of this
951 early and accelerated senescence are not completely understood but may be related to O₃ induced
952 enhanced expression of many genes involved in natural senescence (Miller *et al.*, 1999). Elevated O₃
953 was also found to inhibit sugar export from leaves (Singh Yadav *et al.*, 2020; Feng *et al.*, 2024) which
954 could trigger early onset of leaf senescence.

955 The DO₃SE-Crop model accounts for the impact of O₃ on the Rubisco enzyme by incorporating
956 modified (Ewert and Porter, 2000) functions for instantaneous and long-term O₃ impact on V_{cmax} as
957 an important parameter used to characterize the crop photosynthetic capacity (Ewert and Porter,
958 2000; Osborne *et al.*, 2019). The DO₃SE-Crop model assumes that the O₃ will only accumulate on
959 exceedance of a stomatal O₃ flux threshold of 6 nmol O₃ m⁻² s⁻¹. The long-term O₃ impact mechanism
960 of the DO₃SE-Crop model simulated the effect of senescence on V_{cmax} reasonably well as evidenced
961 by the reduction in leaf chlorophyll content. We used the breakpoint method (Yang *et al.*, 2016;
962 Mariën *et al.*, 2019) to estimate the SOS and EOS using the day of the year and measured
963 chlorophyll content (Fig. 7 and Fig. S4). It is crucial to accurately model the timing of SOS and EOS
964 correctly as this determines the O₃ effect on the duration of the grain filling period and hence the
965 difference in yield loss due to different O₃ treatments. For example, we modelled a difference of 3 to
966 5 in SOS, and 6 to 9 days in EOS, on average across years for the sensitive and tolerant cultivar
967 respectively.

968 China's wheat breeding programme has seen more than 1,850 varieties used across China between
969 the 1920s to 2014 leading to increased yields from less than 1 to more than 5 tonnes ha⁻¹ (Qin *et al.*,
970 2015). Here, albeit with an extremely limited dataset, we parameterise the DO₃SE-Crop model for
971 tolerant and sensitive wheat crop cultivars, since many experimental studies have shown that the
972 response of different cultivars to O₃ stress differs (Biswas *et al.*, 2008). Based on the available data
973 the model seemed able to capture the difference in grain dry matter between these different
974 cultivar groups across different years reasonably well when compared to the observed dataset (R²

975 =0.68; see Fig. 8). Such a cultivar sensitivity-based parametrisation can provide additional
976 information on the certainty of regional yield loss estimates given the large number of wheat
977 varieties grown across China. However, when applying the model to a broader region, it would be
978 advisable to calibrate phenology for different agro-ecological zones as the temperature changes
979 across China, impacting the duration of the key phenological stages such as anthesis and maturity
980 (Luo et.al., 2021). Additionally, carbon allocation parameters may need adjustment, as studies have
981 shown changes in dry matter content across different agro-ecological zones (Hussain and Bagash,
982 2017).

983 **Conclusions**

984 We have shown that the newly developed DO₃SE-Crop model can be calibrated for O₃ tolerant and
985 sensitive wheat varieties for O₃-FACE site conditions at Xioaji in China. The model can simulate crop
986 phenology, leaf physiology, crop growth and yield reasonably well across different years. The model
987 is also able to simulate the effect of O₃ stress on grain yield distinguishing the extent of O₃ damage
988 resulting from the same O₃ treatment on cultivars with differing O₃ sensitivities. The DO₃SE-Crop
989 model also has the advantage of simulating O₃ transfer and deposition dynamics within the wheat
990 crop canopy which could in the future improve our understanding of whole canopy O₃ effects for
991 crops with different carbon allocation profiles. The ability of the model to estimate relative yield
992 losses across years also suggests the model is 'fit for purpose' to assess the effects of O₃ under a
993 variety of climate variable and O₃ concentration conditions.

Appendix A

A1. DO₃SE-Crop variables

Variable	Unit	Description
T_{eff}	°C days	Effective temperature accumulated between sowing to maturity
DVI	-	Development index
T_{air}	°C	Surface air temperature in degrees Celsius
$T_{air,k}$	degrees Kelvin	Surface air temperature in Kelvin
T_{min}	°C	Daily minimum surface air temperature
T_{max}	°C	Daily maximum surface air temperature
LTT	°C d	Thermal time accumulated by a leaf
V_{dd}	days	Accumulated vernalised days
V	days	Vernalised days
V_d	days	Devernalised days
VF	-	Vernalisation factor
PP	hrs	Photoperiod
PF	-	Photoperiod factor
A_{net}	$\mu\text{mol CO}_2 \text{ m}^{-2} \text{ s}^{-1}$	Net photosynthesis or rate of CO ₂ assimilation
A_c	$\mu\text{mol CO}_2 \text{ m}^{-2} \text{ s}^{-1}$	RuBP (ribulose-1,5-bisphosphate) limited A_{net}
A_j	$\mu\text{mol CO}_2 \text{ m}^{-2} \text{ s}^{-1}$	Electron transport limited A_{net}
A_p	$\mu\text{mol CO}_2 \text{ m}^{-2} \text{ s}^{-1}$	TPU (triose phosphate) limited A_{net}
R_d	$\mu\text{mol CO}_2 \text{ m}^{-2} \text{ s}^{-1}$	Dark respiration
f_{PAW}	-	Fraction of plant available water
PAW_t	-	Threshold of PAW, above which g_{sto} is at a maximum as described f_{PAW} function
PAW	m^3/m^3	Plant available water
C_i	$\mu\text{mol}/\text{mol}$	Intercellular CO ₂ partial pressure
O_i	mmol/mol	Intercellular O ₂ concentrations
Γ^*	$\mu\text{mol}/\text{mol}$	CO ₂ compensation point in the absence of respiration
Γ	$\mu\text{mol}/\text{mol}$	CO ₂ compensation point
J	$\mu\text{mol CO}_2 \text{ m}^{-2} \text{ s}^{-1}$	electron transport rate
VPD	kPa	Leaf to air vapour pressure deficit
C_z	ppb	O ₃ concentration at reference height z
C_h	nmol/m^3	O ₃ concentration at the crop canopy height
C_{zh}	nmol/m^3	O ₃ concentration at the top of the crop canopy height
C_{zb}	nmol/m^3	O ₃ concentration at the bottom of the crop canopy height
f_{st}	$\text{nmol O}_3 \text{ m}^{-2} \text{ s}^{-1}$	Leaf level stomatal O ₃ flux
$accf_{st}$	$\text{mmol O}_3 \text{ m}^{-2}$	Accumulated stomatal O ₃ flux
C_l	$\text{nmol O}_3 \text{ m}^{-3}$	O ₃ at the upper surface of the laminar layer of a leaf

$f_{O_3,s}(d)$	-	Effect of daily cumulative stomatal O_3 flux on $V_{c_{max}}$
$f_{O_3,s}(h)$	-	Effect of hourly cumulative stomatal O_3 flux on $V_{c_{max}}$
$f_{O_3,s}(d - 1)$	-	Previous days effect of cumulative stomatal O_3 flux on $V_{c_{max}}$
$r_{O_3,s}$	-	Incomplete overnight recovery of O_3 affected $V_{c_{max}}$
f_{LA}	-	Leaf age related capacity to recover from accumulated stomatal O_3 flux
f_{O_3}	-	Weighted accumulated stomatal O_3 flux that determines the onset of leaf senescence
f_{LS}	-	Accumulated stomatal O_3 flux effect on leaf senescence
tl	°C days	Effective temperature accumulated by a leaf after emergence ($DVI = 0$)
tl_{ep}	-	Effective temperature accumulated by a leaf between full expansion and the onset of leaf senescence
tl_{epO_3}	-	Effective temperature accumulated by a leaf between full expansion and the onset of leaf senescence brought forward by O_3
tl_{se}	-	Effective temperature accumulated by a leaf between the onset of leaf senescence and maturity
tl_{seO_3}	-	Effective temperature accumulated by a leaf between the onset of leaf senescence and maturity brought forward by O_3
g_{CO_2}	$\mu\text{mol CO}_2 \text{ PLA m}^{-2} \text{ s}^{-1}$	Stomatal conductance to CO_2
f_{VPD}	-	Relationship between VPD and relative stomatal conductance
c_s	$\text{mol CO}_2/\text{mol}$	External CO_2 concentration at the leaf surface
c_a	$\text{mmol CO}_2/\text{mol}$	external CO_2 concentration at the upper surface of the leaf boundary layer
g_{bCO_2}	$\text{mol m}^{-2} \text{ s}^{-1}$	Quasi laminar boundary layer conductance to CO_2
C_z	$\text{nmol O}_3 \text{ m}^{-3}$	O_3 concentration at reference height (z)
C_l	$\text{nmol O}_3 \text{ m}^{-3}$	O_3 concentration at the upper surface of the laminar layer of a leaf
g_{O_3}	$\text{mmol O}_3 \text{ PLA m}^{-2} \text{ s}^{-1}$	Stomatal conductance to O_3
$g_{O_3m/s}$	m/s	Stomatal conductance to O_3
g_{ext}	m/s	External conductance
r_c	s/m	Leaf surface resistance to O_3
r_{b,O_3}	s/m	Quasi laminar leaf boundary layer resistance to O_3
r_a	s/m	Atmospheric resistance to O_3
r_{inc}	s/m	In-canopy resistance to O_3
r_{ext}	s/m	External plant cuticle resistance to O_3
r_{sto}	s/m	Stomatal resistance to O_3
u_z	m/s	Wind speed at a reference height z
u_l	m/s	Wind speed at the upper surface of the laminar layer of a leaf
L	m	Cross wind leaf dimension
LAI	$\text{m}^2 \text{ m}^{-2}$	Leaf Area Index
$PAR_{dir,i}$	W/m^2	Direct PAR in canopy layer i
$PAR_{diff,i}$	W/m^2	Diffuse PAR in canopy layer i
PAR_{total}	W/m^2	Direct and diffuse PAR at the top of the canopy

NPP	kg C m ⁻²	Net primary productivity
GPP	kg C m ⁻²	Gross primary productivity
R_p	kg C m ⁻²	Plant respiration
R_{pm}	kg C m ⁻²	Plant maintenance respiration
R_{pg}	kg C m ⁻²	Plant growth respiration
A_{netc}	kg C m ⁻²	Canopy net photosynthesis
R_{dc}	kg C m ⁻²	Non-water stressed canopy dark respiration
$f_{sw}R_{dc}$	kg C m ⁻²	Water stressed modified canopy dark respiration
C_{root}	kg C m ⁻²	Root C pool
C_{leaf}	kg C m ⁻²	Leaf C pool
C_{stem}	kg C m ⁻²	Stem C pool
C_{resv}	kg C m ⁻²	Reserve C pool
C_{harv}	kg C m ⁻²	Harvest pool
P_{root}	-	Root C pool partition coefficient
P_{leaf}	-	Leaf C pool partition coefficient
P_{stem}	-	Stem C pool partition coefficient
P_{resv}	-	Reserve C pool partition coefficient
P_{harv}	-	Harvest C pool partition coefficient
$C_{leaf,green}$	kg C m ⁻²	Green leaf C
$C_{leaf,brown}$	kg C m ⁻²	Brown leaf C
SLA	m ² kg ⁻¹	Specific Leaf Area
h	m	Crop height
$Yield_{grain}$	g C m ⁻²	Grain yield
k_p'	-	Beam and scattered beam PAR extinction coefficient
k_d'	-	Diffuse and scattered diffuse PAR extinction coefficient
ρ_{cb}	-	Canopy reflection coefficient for beam PAR
ρ_{cd}	-	Canopy reflection coefficient for diffuse PAR
β	Radians	Solar elevation angle
δ	Radians	Solar declination angle
$PAR_{dir} (LAI)$	$\mu\text{mol m}^{-2} \text{s}^{-1}$	Absorbed beam plus scattered beam PAR per unit leaf area
$PAR_{diff} (LAI)$	$\mu\text{mol m}^{-2} \text{s}^{-1}$	Absorbed diffuse plus scattered diffuse PAR per unit leaf area
$PAR (LAI)$	$\mu\text{mol m}^{-2} \text{s}^{-1}$	Total absorbed PAR per unit leaf area
$I_b (LAI)$	$\mu\text{mol m}^{-2} \text{s}^{-1}$	Direct PAR per unit ground area
$I_d (LAI)$	$\mu\text{mol m}^{-2} \text{s}^{-1}$	Diffuse PAR per unit ground area
$I_d (0)$	$\mu\text{mol m}^{-2} \text{s}^{-1}$	Diffuse PAR per unit ground area at the top of the canopy
$I_b (0)$	$\mu\text{mol m}^{-2} \text{s}^{-1}$	Beam PAR per unit ground area at the top of the canopy
$PAR_{ps} (LAI)$	$\mu\text{mol m}^{-2} \text{s}^{-1}$	Absorbed scattered beam PAR per unit leaf area
$PAR_{psun} (LAI)$	$\mu\text{mol m}^{-2} \text{s}^{-1}$	Beam PAR absorbed by sunlit leaves per unit leaf area

PAR_{sh} (LAI)	$\mu mol m^{-2} s^{-1}$	Beam PAR absorbed byshaded leaves per unit leaf area
PAR_{sun} (LAI)	$\mu mol m^{-2} s^{-1}$	Total PAR absorbed by sunlit leaves per unit leaf area
PAR_{total}	$\mu mol m^{-2} s^{-1}$	Total absorbed irradiance per unit leaf area
LAI	$m^2 m^{-2}$	Cumulative leaf area index from top of canopy (L=0 at top)
$f_{1,2}$ (LAI)	-	Fraction of leaf area in a leaf-angle class
LAI _{sh}	-	Fraction of leaves that are shaded
LAI _{sun}	-	Fraction of leaves that are sunlit
σ	-	Leaf scattering coefficient for PAR
α_1	Radians	Angle of beam irradiance to the leaf normal
$\sin\beta$	-	Solar elevation angle
k_b'	-	Beam and scattered beam PAR extinction coefficient
k_d'	-	Diffuse and scattered diffuse PAR extinction coefficient
σ	-	Leaf scattering coefficient for PAR
α_1	Radians	Angle of beam irradiance to the leaf normal

A2. DO₃SE-Crop parameters for wheat. Highlighted are the parameters (and their associated ranges) which require calibration when applying DO₃SE-Crop to varying environmental conditions.

Parameter	Unit	Default Value	Description	Reference	Range	Calibrated Parameter Value
T_b	°C	0	Base temperature	(Tao, Zhang and Zhang, 2012; Osborne <i>et al.</i> , 2015)	-0.5-1	-0.25
T_o	°C	20	Optimum temperature	(Tao, Zhang and Zhang, 2012; Osborne <i>et al.</i> , 2015)	15-25	17.79
T_m	°C	30	Maximum temperature	(Tao, Zhang and Zhang, 2012; Osborne <i>et al.</i> , 2015)	25-40	23.87
TT_{emr}	°C d	100	Thermal time between sowing and emergence	(Lu <i>et al.</i> , 2018; Luo <i>et al.</i> , 2020)	50-100	220.6
TT_{veg}	°C d	940	Thermal time between emergence and anthesis	Xiaoji experimental dataset	400-940	940
TT_{rep}	°C d	304	Thermal time between anthesis and maturity	(Wang <i>et al.</i> , 2013a); Xiaoji experimental dataset	300-650	304
TT_{leaf}	°C d	1000	Total canopy-leaf life span of the crop, covers period from emergence to maturity, distributed over the DVI between 0 and 2	(Lu <i>et al.</i> , 2018; Luo <i>et al.</i> , 2020)	700-1200	795

T_l	°C d	1400	Total lifespan of the crop, covers the full period from sowing to maturity, corresponding to DVI between -1 to 2	(Ewert and Porter, 2000; Lu <i>et al.</i> , 2018; Luo <i>et al.</i> , 2020)	1300-1500	Year 2007- 1325, Year 2008- 1400, Year 2009- 1478.
PIV		1.5	Vernalisation coefficient	(Tao, Zhang and Zhang, 2012; Wang <i>et al.</i> , 2013)	2.9-4	2.9
PID		40	Photoperiod coefficient	(Wang <i>et al.</i> , 2013; Liu <i>et al.</i> , 2016; Zhao <i>et al.</i> , 2020)	40-57	40
VT_{max}	°C	30	Maximum daily temperature for vernalisation	Zheng <i>et al.</i> , 2015		
VT_{min}	°C	15	Minimum daily temperature for vernalisation	Zheng <i>et al.</i> , 2015		
PAW_t	m ³ /m ³	50	Plant available soil water below which stomatal conductance will start to reduce	LRTAP, 2017		
V_{cmax}	μmol CO ₂ m ⁻² s ⁻¹	90	Maximum carboxylation capacity at 25°C	(Büker <i>et al.</i> , 2012)	90-140	137
J_{max}	μmol CO ₂ m ⁻² s ⁻¹	180	Maximum rate of electron transport at 25°C	(Büker <i>et al.</i> , 2012)	180-250	228
K_c	μmol/mol	404.9	Rubisco Michaelis-Menten constants for CO ₂	(Medlyn <i>et al.</i> , 2002)		
K_o	mmol/mol	278.4	Rubisco Michaelis-Menten constants for O ₂	(Medlyn <i>et al.</i> , 2002)		
Γ^*	μmol/mol	42.75	CO ₂ compensation point in the absence of respiration	(Medlyn <i>et al.</i> , 2002)		
a	-	4	Electron requirement for the formation of NADPH	(Sharkey <i>et al.</i> , 2007)		
b	-	8	Electron requirement for the formation of ATP	(Sharkey <i>et al.</i> , 2007)		
R_{dcoeff}	-	0.015	Leaf dark respiration coefficient	(Clark <i>et al.</i> , 2011)	0.010-0.03	0.01
f_{min}	μmol CO ₂ /m ² /s	1000	Minimum daytime stomatal conductance to CO ₂	(Ewert and Porter, 2000)		
m	-	7	composite sensitivity slope constant	(Büker <i>et al.</i> , 2012)	4-15	5
VPD_0	kPa	2.2	stomatal conductance sensitivity to VPD	UNECE, 2017; Pande <i>et al.</i> 2024		
γ_1	-	0.027	O ₃ short-term damage co-efficient	(Ewert and Porter, 2000)		
γ_2	(nmol O ₃ m ⁻² s ⁻¹) ⁻¹	0.0045	O ₃ short-term damage co-efficient	(Ewert and Porter, 2000)		
γ_3	(μmol O ₃ m ⁻²) ⁻¹	0.00005	O ₃ long-term damage co-efficient	(Ewert and Porter, 2000)	0.00001-0.00009	Tolerant=0.00001 Sensitive=0.00002

γ_4	-	5	O ₃ long-term damage co-efficient determining onset of senescence		5-15	Tolerant=5 Sensitive=15
γ_5	-	0.8	O ₃ long-term damage co-efficient determining maturity		0.5-5	Tolerant=0.8 Sensitive=5
$CLsO_3$	mmol O ₃ m ⁻²	6.5-20.6,20.5	Critical accumulated stomatal O ₃ flux that determines the onset of leaf senescence	(Osborne <i>et al.</i> , 2019; Feng <i>et al.</i> , 2022)	3-21	4.2
r_{ext}	m/s	2500	External leaf cuticular resistance to O ₃ uptake	UNECE, 2017		
L	m	0.02	Cross wind leaf dimension for wheat	UNECE, 2017		
P_{st}	Pa	1.013 x 10 ⁵	Standard air pressure at 20°C	UNECE, 2017		
T_{st}	°C	20	Standard temperature	UNECE, 2017		
R	J/mol/K	8.31447	Universal gas constant	UNECE, 2017		
n_e	mol CO ₂ m ⁻² s ⁻¹ kg C (kg N) ⁻¹	0.0008	Constant relating leaf nitrogen to rubisco carboxylation capacity	(Clark <i>et al.</i> , 2011)		
n_0	kg N [kg C] ⁻¹	0.073	Top canopy leaf N concentration	(Clark <i>et al.</i> , 2011)		
kN		0.78	Nitrogen profile co-efficient	(Clark <i>et al.</i> , 2011)		
R_{gcoeff}	-	0.25	Plant growth respiration coefficient	(Osborne <i>et al.</i> , 2015)	0.15-0.25	0.16
α_{root}	-	18.5	Coefficient for determining partitioning	(Osborne <i>et al.</i> , 2015)	16-19	18.4
α_{stem}	-	16.0	Coefficient for determining partitioning	(Osborne <i>et al.</i> , 2015)	16-17	16.8
α_{leaf}	-	18.0	Coefficient for determining partitioning	(Osborne <i>et al.</i> , 2015)	18-19	18.5
β_{root}	--	-20.0	Coefficient for determining partitioning	(Osborne <i>et al.</i> , 2015)	20-21	-20.9
β_{stem}	-	-15.0	Coefficient for determining partitioning	(Osborne <i>et al.</i> , 2015)	14-16	-14.5
β_{leaf}	-	-18.5	Coefficient for determining partitioning	(Osborne <i>et al.</i> , 2015)	18-19	-18.11
f_c	-	0.5	Carbon fraction of dry matter	(Osborne <i>et al.</i> , 2015)		
Υ	m ⁻² kg ⁻¹	27.3	Coefficient for determining specific leaf area	(Osborne <i>et al.</i> , 2015)	13-28	13.5
δ	-	-0.0507	Coefficient for determining specific leaf area	(Osborne <i>et al.</i> , 2015)		
k	-	1.4	allometric coefficient which relates C_{stem} to h	(Osborne <i>et al.</i> , 2015)		
τ	-	0.4	allometric coefficient which relates C_{stem} to h	(Osborne <i>et al.</i> , 2015)	0.3-0.6	0.4

D_w	-	1/0.84	Conversion factor to allow for grain moisture content	(Mulvaney and Devkota, 2020)		
E_g	-	0.85	Conversion factor for grain to ear ratio	(Nagarajan <i>et al.</i> , 1999; Kutman, Yildiz and Cakmak, 2011)		
R_{SL}	-	2:1	Stem dry matter to leaf dry matter ratio	(Huang et al., 2022)		
k_b'	-	$0.46/\sin\beta$	Beam and scattered beam PAR extinction coefficient	(Pury and Farquhar,1997)		
k_d'	-	0.8	Diffuse and scattered diffuse PAR extinction coefficient	(Pury and Farquhar,1997)		
σ	-	0.15	Leaf scattering coefficient for PAR	(Pury and Farquhar,1997)		
α_1	Radians	0.5	Angle of beam irradiance to the leaf normal	(Pury and Farquhar,1997)		

References

- Amthor, J. S., Bar-Even, A., Hanson, A. D., Millar, A. H., Stitt, M., Sweetlove, L. J., and Tyerman, S. D.: Engineering strategies to boost crop productivity by cutting respiratory carbon loss, *Plant Cell*, 31(2), 297–314, <https://doi.org/10.1105/tpc.18.00743>, 2019.
- Betzelberger, A. M., Gillespie, K. M., McGrath, J. M., Koester, R. P., Nelson, R. L., and Ainsworth, E. A.: Ozone exposure response for U.S. soybean cultivars: Linear reductions in photosynthetic potential, biomass, and yield, *Plant Physiology*, American Society of Plant Biologists, 160(4), 1827–1839, <https://doi.org/10.1104/pp.112.205591>, 2012.
- Beven, K.: A manifesto for the equifinality thesis. *Journal of Hydrology*, 320(1–2), 18–36. <https://doi.org/10.1016/j.jhydrol.2005.07.007>, 2006.
- Biswas, D. K., Xu, H., Li, Y. G., Sun, J. Z., Wang, X. Z., Han, X. G., and Jiang, G. M.: Assessing the genetic relatedness of higher ozone sensitivity of modern wheat to its wild and cultivated progenitors/relatives, *Journal of Experimental Botany*, 59(4), 951–963, <https://doi.org/10.1093/jxb/ern022>, 2008.
- Brewster, C., Fenner, N., and Hayes, F.: Chronic ozone exposure affects nitrogen remobilization in wheat at key growth stages, *Science of The Total Environment*, Elsevier B.V., 908(August 2023), 168288, <https://doi.org/10.1016/j.scitotenv.2023.168288>, 2024.
- Brewster, C., Hayes, F., and Fenner, N.: Ozone Tolerance Found in *Aegilops tauschii* and Primary Synthetic Hexaploid Wheat, *Plants*, 8(7), 195, <https://doi.org/10.3390/plants8070195>, 2019.
- Büker, P., Morrissey, T., Briolat, A., Falk, R., Simpson, D., Tuovinen, J.-P., Alonso, R., Barth, S., Baumgarten, M., Grulke, N., Karlsson, P. E., King, J., Lagergren, F., Matyssek, R., Nunn, A., Ogaya, R., Peñuelas, J., Rhea, L., Schaub, M., Uddling, J., Werner, W., and Emberson, L. D.: DO3SE modelling of soil moisture to determine ozone flux to forest trees, *Atmospheric Chemistry and Physics*, 12(12), 5537–5562, <https://doi.org/10.5194/acp-12-5537-2012>, 2012
- Campbell, G. S., and Norman, J. M.: An introduction to Environmental Biophysics, Second Edition, Springer, 1998.
- Challinor, A. J., Watson, J., Lobell, D. B., Howden, S. M., Smith, D. R., and Chhetri, N.: A meta-analysis of crop yield under climate change and adaptation, *Nature Climate Change*, 4(4), 287–291, <https://doi.org/10.1038/nclimate2153>, 2014.
- Clark, D. B., Mercado, L. M., Sitch, S., Jones, C. D., Gedney, N., Best, M. J., Pryor, M., Rooney, G. G., Essery, R. L. H., Blyth, E., Boucher, O., Harding, R. J., Huntingford, C., and Cox, P. M.: The Joint UK Land Environment Simulator (JULES), model description – Part 2: Carbon fluxes and vegetation dynamics, *Geoscientific Model Development*, 4(3), 701–722, <https://doi.org/10.5194/gmd-4-701-2011>, 2011.
- Conibear, L., Butt, E. W., Knote, C., Spracklen, D. V., and Arnold, S. R.: Current and Future Disease Burden From Ambient Ozone Exposure in India, *GeoHealth*, 2, 334–355, <https://doi.org/10.1029/2018GH000168>, 2018.
- Danielsson, H., Karlsson, G. P., Karlsson, P. E., and Pleijel, H. H.: Ozone uptake modelling and flux-response relationships—an assessment of ozone-induced yield loss in spring wheat. *Atmospheric Environment*, 37(4), 475–485, [https://doi.org/10.1016/S1352-2310\(02\)00954-7](https://doi.org/10.1016/S1352-2310(02)00954-7), 2003.

Dentener, F., Emberson, L., Galmarini, S., Cappelli, G., Irimescu, A., Mihailescu, D., Van Dingenen, R., van den Berg, M.: Lower air pollution during COVID-19 lock-down: improving models and methods estimating ozone impacts on crops. *Philosophical Transactions of the Royal Society A: Mathematical, Physical and Engineering Sciences* 378, 20200188. <https://doi.org/10.1098/rsta.2020.0188>, 2020.

Droutsas, I., Challinor, A. J., Arnold, S. R., Mikkelsen, T. N., and Hansen, E. M. Ø.: A new model of ozone stress in wheat including grain yield loss and plant acclimation to the pollutant. *European Journal of Agronomy*, 120, 126125. <https://doi.org/10.1016/j.eja.2020.126125>, 2020.

Emberson, L. D., Ashmore, M. R., Simpson, D., Tuovinen, J.-P., and Cambridge, H. M.: Modelling and mapping ozone deposition in Europe, *Water, Air and Soil Pollution*, 577–582, 2001.

Emberson, L. D., Ashmore, M. R., Cambridge, H. M., Simpson, D., and Tuovinen, J.-P.: Modelling stomatal ozone flux across Europe, *Environmental Pollution*, 109(3), 403–413, [https://doi.org/10.1016/S0269-7491\(00\)00043-9](https://doi.org/10.1016/S0269-7491(00)00043-9), 2000.

Emberson, L. D., Pleijel, H., Ainsworth, E. A., van den Berg, M., Ren, W., Osborne, S., Mills, G., Pandey, D., Dentener, F., Büker, P., Ewert, F., Koeble, R., and Van Dingenen, R.: Ozone effects on crops and consideration in crop models, *European Journal of Agronomy*, Elsevier, 100(May), 19–34, <https://doi.org/10.1016/j.eja.2018.06.002>, 2018.

Ewert, F., and Porter, J. R.: Ozone effects on wheat in relation to CO₂: Modelling short-term and long-term responses of leaf photosynthesis and leaf duration, *Global Change Biology*, 6(7), 735–750, <https://doi.org/10.1046/j.1365-2486.2000.00351.x>, 2000.

Farage, P. K., Long, S. P., Lechner, E. G., and Baker, N. R.: The sequence of change within the photosynthetic apparatus of wheat following short-term exposure to ozone, *Plant Physiology*, 95(2), 529–535, <https://doi.org/10.1104/pp.95.2.529>, 1991.

Farquhar, G. D., von Caemmerer, S., and Berry, J. A.: A biochemical model of photosynthetic CO₂ assimilation in leaves of C₃ species, *Planta*, 149, 78–90, <https://doi.org/10.1007/BF00386231>, 1980.

Feng, Y., Nguyen, T. H., Alam, M. S., Emberson, L., Gaiser, T., Ewert, F., and Frei, M.: Identifying and modelling key physiological traits that confer tolerance or sensitivity to ozone in winter wheat, *Environmental Pollution*, Elsevier Ltd, 304(April), 119251, <https://doi.org/10.1016/j.envpol.2022.119251>, 2022.

Feng, Y., Alam, M. S., Yan, F., Frei, M.: Alteration of carbon and nitrogen allocation in winter wheat under elevated ozone, *Plant Science*, Elsevier, 338, 111924, <https://doi.org/10.1016/j.plantsci.2023.111924>, 2024.

Feng, Z., Pang, J., Kobayashi, K., Zhu, J., OTR, R.D.: Differential responses in two varieties of winter wheat to elevated ozone concentration under fully open-air field conditions, *Global Change Biology*, 17(1), 580–591, <https://doi.org/10.1111/j.1365-2486.2010.02184.x>, 2011.

Feng, Z., Tang, H., Uddling, J., Pleijel, H., Kobayashi, K., Zhu, J., Oue, H., Guo, W.: A stomatal ozone flux-response relationship to assess ozone-induced yield loss of winter wheat in subtropical China, *Environmental Pollution*, Elsevier Ltd, 164, 16–23, <https://doi.org/10.1016/j.envpol.2012.01.014>, 2012.

Feng, Z., Wang, L., Pleijel, H., Zhu, J., Kobayashi, K.: Differential effects of ozone on photosynthesis of winter wheat among cultivars depend on antioxidative enzymes rather than stomatal conductance, *The Science of the Total Environment*, 572, 404–411, <https://doi.org/10.1016/j.scitotenv.2016.08.083>, 2016.

Feng, Z., Uddling, J., Tang, H., Zhu, J., and Kobayashi, K.: Comparison of crop yield sensitivity to ozone between open-top chamber and free-air experiments, *Global Change Biology*, 24(6), 2231–2238, <https://doi.org/10.1111/gcb.14077>, 2018.

Feng, Z., Agathokleous, E., Yue, X., Oksanen, E., Paoletti, E., Sase, H., Gandin, A., Koike, T., Calatayud, V., Yuan, X., Liu, X., De Marco, A., Jolivet, Y., Kontunen-Soppela, S., Hoshika, Y., Saji, H., Li, P., Li, Z., Watanabe, M., & Kobayashi, K.: *Emerging challenges of ozone impacts on Asian plants: Actions are needed to protect ecosystem health*. *Ecosystem Health and Sustainability*, 7(1), 1911602. <https://doi.org/10.1080/20964129.2021.1911602>, 2021.

Feng, Z., Xu, Y., Kobayashi, K., Dai, L., Zhang, T., Agathokleous, E., Calatayud, V., Paoletti, E., Mukherjee, A., Agrawal, M., Park, R. J., Oak, Y. J., and Yue, X.: *Ozone pollution threatens the production of major staple crops in East Asia*, *Nature Food*, 3, 47–56, <https://doi.org/10.1038/s43016-021-00422-6>, 2022..

Feng, Y., Nguyen, T. H., Alam, M. S., Emberson, L., Gaiser, T., Ewert, F., and Frei, M.: Identifying and modelling key physiological traits that confer tolerance or sensitivity to ozone in winter wheat, *Environmental Pollution*, 304, 119251, <https://doi.org/10.1016/j.envpol.2022.119251>, 2022.

Gelang, J., Pleijel, H., Sild, E., Danielsson, H., Younis, S., Selldén, G., and Wallin, G.: Rate and duration of grain filling in relation to flag leaf senescence and grain yield in spring wheat (*Triticum aestivum*) exposed to different concentrations of ozone, *Physiologia Plantarum*, 110(3), 366–375, <https://doi.org/10.1111/j.1399-3054.2000.1100311.x>, 2000.

Graham, A., Pope, R., Pringle, K., Arnold, S., Chipperfield, M., Conibear, L., Butt, E., Kiely, L., Knotte, C., and McQuaid, J.: Impact on air quality and health due to the Saddleworth Moor fire in northern England, *Environmental Research Letters*, 15(7), 074001, <https://doi.org/10.1088/1748-9326/ab8496>, 2020.

Graham, A., Pringle, K., Pope, R., Arnold, S., Conibear, L., Burns, H., Rigby, R., Borchers-Arriagada, N., Butt, E., Kiely, L., Reddington, C., Spracklen, D., Woodhouse, M., Knotte, C., and McQuaid, J.: Impact of the 2019/2020 Australian Megafires on Air Quality and Health, *GeoHealth*, 5(10), e2021GH000454, <https://doi.org/10.1029/2021GH000454>, 2021.

Grandjean, A., and Fuhrer, J.: Growth and leaf senescence in spring wheat (*Triticum aestivum*) grown at different ozone concentrations in open-top field chambers, *Environmental Pollution*, 59, 299–314, 1989.

Guan, X., Song, L., Wang, T. C., Turner, N., and Li, F.: Effect of Drought on the Gas Exchange, Chlorophyll Fluorescence and Yield of Six Different-Era Spring Wheat Cultivars, *Journal of Agronomy and Crop Science*, 201(4), 253–266, <https://doi.org/10.1111/jac.12103>, 2015.

Guarin, J. R., Kassie, B., Mashaheet, A. M., Burkey, K., and Asseng, S.: Modeling the effects of tropospheric ozone on wheat growth and yield, *European Journal of Agronomy*, 105, 13–23, <https://doi.org/10.1016/j.eja.2019.03.001>, 2019.

Guarin, J. R., Jägermeyr, J., Ainsworth, E. A., Oliveira, F. A. A., Asseng, S., Boote, K., Elliott, J., Emberson, L., Foster, I., Hoogenboom, G., Kelly, D., Ruane, A. C., and Sharps, K.: Modeling the effects

of tropospheric ozone on the growth and yield of global staple crops with DSSAT v4.8.0, *Geoscientific Model Development*, 17, 2547–2567, <https://doi.org/10.5194/gmd-17-2547-2024>, 2024.

Herman, J., and Usher, W.: SALib: An open-source Python library for sensitivity analysis, *J. Open Source Softw.*, 2(9), <https://doi.org/10.21105/joss.00097>, 2017.

Huang, H., Huang, J., Li, X., Feng, J., Zhuo, W., Wu, Y., Niu, Q., Su, W., and Yin, Y.: A dataset of winter wheat aboveground biomass in China during 2007–2015 based on data assimilation, *Scientific Data*, Springer US, 9(1), 1–11, <https://doi.org/10.1038/s41597-022-01305-6>, 2022.

Hussain, A., and Bangash, R.: Impact of Climate Change on Crops' Productivity across Selected Agro-ecological Zones in Pakistan, *The Pakistan Development Review*, 56(2), 163–187, <https://www.jstor.org/stable/26875191>, 2017.

Jaggi, M., Ammann, C., Neftel, J., and Fuhrer, J.: Environmental control of profiles of ozone concentration in a grassland canopy, *Atmospheric Environment*, 40(28), 5496–5507, <https://doi.org/10.1016/j.atmosenv.2006.01.025>, 2006.

Jones, H. G.: *Plants and microclimate: A quantitative approach to environmental plant physiology*, Cambridge University Press, 1992.

Kohut, R. J., Amundson, R. G., Laurence, J. A., Colavito, L., van Leuken, P., and King, P.: Effects of Ozone and Sulfur Dioxide on Yield of Winter Wheat, *Phytopathology*, 77, 71–74, <https://doi.org/10.1094/Phyto-77-71>, 1987.

Konduri, V. S., Tomas, V. J., Ganguly, S., and Ganguly, A. R.: Data Science for Weather Impacts on Crop Yield, *Frontiers in Sustainable Food Systems*, 4(May), 52, <https://doi.org/10.3389/fsufs.2020.00052>, 2020.

Lee, J. D., Drysdale, W. S., Finch, D. P., Wilde, S. E., and Palmer, P. I.: UK surface NO₂ levels dropped by 42% during the COVID-19 lockdown: Impact on surface O₃, *Atmospheric Chemistry and Physics*, 20(24), 15743–15759, <https://doi.org/10.5194/acp-20-15743-2020>, 2020.

Leung, F., Williams, K. E., Sitch, S., Tai, A. P. K., Wiltshire, A., Gornall, J., Ainsworth, E. A., Arkebauer, T., and Scoby, D.: Calibrating soybean parameters in JULES 5.0 from the US-Ne2/3 FLUXNET sites and the SoyFACE-O₃ experiment, *Geoscientific Model Development*, 13(12), 6201–6213, <https://doi.org/10.5194/gmd-13-6201-2020>, 2020.

IPCC: *Climate Change 2021: The Physical Science Basis. Contribution of Working Group I to the Sixth Assessment Report of the Intergovernmental Panel on Climate Change*, Cambridge University Press, <https://doi.org/10.1017/9781009157896>, 2021

Leuning, R.: Modeling stomatal behavior and photosynthesis of *Eucalyptus grandis*, *Australian Journal of Plant Physiology*, 17(2), 159–175, 1990.

Leuning, R.: A critical appraisal of combined stomatal models for C₃ plants, *Plant, Cell & Environment*, 18(4), 339–355, 1995. Available at: <http://www.unc.edu/courses/2010spring/geog/595/001/www/Leuning95b-PCE.pdf>.

Li, A., Zhou, Q., and Xu, Q.: Prospects for ozone pollution control in China: An epidemiological perspective, *Environmental Pollution*, 285, 117670, <https://doi.org/10.1016/j.envpol.2021.117670>, 2021.

- Li, D., Shindell, D., Ding, D., Xiao, Lu., Zhang, L., and Zhang, Y.: Surface ozone impacts on major crop production in China from 2010 to 2017, *Atmospheric Chemistry and Physics*, 22(4), 2625–2638, <https://doi.org/10.5194/acp-22-2625-2022>, 2022.
- Li, K., Jacob, D. J., Shen, L., Lu, X., De Smedt, I., and Liao, H.: Increases in surface ozone pollution in China from 2013 to 2019: anthropogenic and meteorological influences, *Atmospheric Chemistry and Physics*, 20(19), 11423–11433, <https://doi.org/10.5194/acp-20-11423-2020>, 2020.
- Lin, M., Horowitz, L. W., Payton, R., Fiore, A. M., and Tonnesen, G.: US surface ozone trends and extremes from 1980 to 2014: Quantifying the roles of rising Asian emissions, domestic controls, wildfires, and climate, *Atmospheric Chemistry and Physics*, 17(4), 2943–2970, <https://doi.org/10.5194/acp-17-2943-2017>, 2017.
- Lim, P. O., Kim, H. J., and Nam, H. G.: Leaf senescence, *Annu. Rev. Plant Biol.*, 58, 115–136, <https://doi.org/10.1146/annurev.arplant.57.032905.105316>, 2007.
- Liu, S., Mo, X., Lin, Z., Xu, Y., Ji, J., Wen, G., and Richey, J.: Crop yield responses to climate change in the Huang-Huai-Hai Plain of China, *Agricultural Water Management*, 97(8), 1195–1209, <https://doi.org/10.1016/j.agwat.2010.03.012>, 2010.
- Liu, Z., Doherty, R. M., Wild, O., O’Connor F. M., and Turnock, T. S.: Tropospheric ozone changes and ozone sensitivity from the present day to the future under shared socio-economic pathways, *Atmospheric Chemistry and Physics*, 22(2), 1209–1227, <https://doi.org/10.5194/acp-22-1209-2022>, 2022.
- Malhi, G. S., Kaur, M., and Kaushik, P.: Impact of Climate Change on Agriculture and Its Mitigation Strategies: A Review, *Sustainability*, 13(3), 1318, <https://doi.org/10.3390/su13031318>, 2021.
- Mariën, B., Balzarolo, M., Dox, I., Leys, S., Marchand J. L., Géron, C., Portillo-Estrada, M., AbdElgawad, H., Asard, H., and Campioli, M.: Detecting the onset of autumn leaf senescence in deciduous forest trees of the temperate zone, *New Phytologist*, 224(1), 166–176, <https://doi.org/10.1111/nph.15991>, 2019.
- Masutomi, Y.: The appropriate analytical solution for coupled leaf photosynthesis and stomatal conductance models for C3 plants, *Ecological Modelling*, 481, 110306, <https://doi.org/10.1016/j.ecolmodel.2023.110306>, 2023.
- Medlyn, B. E., Dreyer, E., Ellsworth, D., Forstreuter, M., Harley, P., Kirschbaum, M., Roux, X., Montpied, P., Strassmeyer, J., Walcroft, A., Wang, K., and Loustau, D.: Temperature response of parameters of a biochemically based model of photosynthesis. II. A review of experimental data, *Plant, Cell and Environment*, 25(9), 1167–1179, <https://doi.org/10.1046/j.1365-3040.2002.00891.x>, 2002
- Miller, J. D., Arteca, R. N., and Pell, E. J.: Senescence-Associated Gene Expression during Ozone-Induced Leaf Senescence in Arabidopsis, *Plant Physiology*, 120(4), 1015, <https://doi.org/10.1104/pp.120.4.1015>, 1999.
- Muhie, S. H.: Novel approaches and practices to sustainable agriculture, *Journal of Agriculture and Food Research*, 10, 100446, <https://doi.org/10.1016/j.jafr.2022.100446>, 2022.
- Mulvaney, M. J., and Devkota, P. J.: Adjusting Crop Yield to a Standard Moisture Content, EDIS, University of Florida George A Smathers Libraries, 2020(3), <https://doi.org/10.32473/edis-ag442-2020>, 2020.

Nguyen, T.H., Cappelli, G.A., Emberson, L., Ignacio, G.F., Irimescu, A., Francesco, S., Fabrizio, G., Booth, N., Boldeanu, G., Bermejo, V., Bland, S., Frei, M., Ewert, F., Gaiser, T.: Assessing the spatio-temporal tropospheric ozone and drought impacts on leaf growth and grain yield of wheat across Europe through crop modeling and remote sensing data. *European Journal of Agronomy* 153, 127052. <https://doi.org/10.1016/j.eja.2023.127052>, 2024.

LRTAP: Mapping critical levels for vegetation, chapter III of manual on methodologies and criteria for modelling and mapping critical loads and levels and air pollution effects, risks and trends, UNECE Convention on Long-range Transboundary Air Pollution, 2017

Van Oijen, M., and Ewert, F.: The effects of climatic variation in Europe on the yield response of spring wheat cv. Minaret to elevated CO₂ and O₃: an analysis of open-top chamber experiments by means of two crop growth simulation models, *European Journal of Agronomy*, 10(3–4), 249–264, [https://doi.org/10.1016/s1161-0301\(99\)00014-3](https://doi.org/10.1016/s1161-0301(99)00014-3), 1999.

Osborne, S., Pandey, D., Mills, G., Hayes, F., Harmens, H., Gillies, D., Bücken, P., and Emberson, L.: New Insights into Leaf Physiological Responses to Ozone for Use in Crop Modelling, *Plants*, 8(4), 84, <https://doi.org/10.3390/plants8040084>, 2019.

Osborne, T., Gornall, J., Hooker, J., Williams, K. E., Wiltshire, A., Betts, R., and Wheeler, T.: JULES-crop: A Parametrisation of Crops in the Joint UK Land Environment Simulator, *Geoscientific Model Development*, 8(4), 1139–1155, <https://doi.org/10.5194/gmd-8-1139-2015>, 2015.

Pande, P., Hayes, F., Bland, S., Booth, N., Pleijel, H., and Emberson, L. D.: Ozone Dose-Response Relationships for Wheat Can Be Derived Using Photosynthetic-Based Stomatal Conductance Models, *Agricultural and Forest Meteorology*, 356, 110150, <https://doi.org/10.1016/j.agrformet.2024.110150>, 2024.

Pleijel, H., Danielsson, H., Emberson, L., Ashmore, M., and Mills, G.: Ozone Risk Assessment for Agricultural Crops in Europe: Further Development of Stomatal Flux and Flux–Response Relationships for European Wheat and Potato, *Atmospheric Environment*, 41(14), 3022–3040, <https://doi.org/10.1016/j.atmosenv.2006.12.002>, 2007.

Pury, D. G. G., and Farquhar, G. D.: Simple Scaling of Photosynthesis from Leaves to Canopies Without the Errors of Big-Leaf Models, *Functional Plant Biology*, 24(5), 537–557, <https://doi.org/10.1071/pp97030>, 1997.

Qin, X., Zhang, F., Liu, C., Yu, H., Cao, B., Tian, S., Liao, Y., and Siddique, K.: Wheat Yield Improvements in China: Past Trends and Future Directions, *Field Crops Research*, 177, 117–124, <https://doi.org/10.1016/j.fcr.2015.03.013>, 2015.

Schauberger, B., Rolinski, S., Schaphoff, S., and Müller, C.: Global Historical Soybean and Wheat Yield Loss Estimates from Ozone Pollution Considering Water and Temperature as Modifying Effects, *Agricultural and Forest Meteorology*, 265, 1–15, <https://doi.org/10.1016/j.agrformet.2018.11.004>, 2019.

Sharkey, T. D., Bernacchi, C. J., Farquhar, G. D., and Singaas, E. L.: Fitting Photosynthetic Carbon Dioxide Response Curves for C₃ Leaves, *Plant, Cell and Environment*, 30(9), 1035–1040, <https://doi.org/10.1111/j.1365-3040.2007.01710.x>, 2007.

Sillmann, J., Aunan, K., Emberson, L., Bücken, P., van Oort, B. V., O'Neill, C., Otero, N., Pandey, D., and Brisebois, A.: Combined Impacts of Climate and Air Pollution on Human Health and Agricultural

Productivity, *Environmental Research Letters*, 16(9), 074001, <https://doi.org/10.1088/1748-9326/ac1df8>, 2021.

Simpson, D., Benedictow, A., Berge, H., Bergström, R., Emberson, L. D., Fagerli, H., Flechard, C. R., Hayman, G., Gauss, M., Jonson, J. E., Jenkin, M. E., Nyíri, Á., Richter, C., Semeena, V. S., Tsyro, S., Tuovinen, J.-P., Valdebenito, Á., and Wind, P.: The EMEP MSC-W Chemical Transport Model – Technical Description, *Atmospheric Chemistry and Physics*, 12(16), 7825–7865, <https://doi.org/10.5194/acp-12-7825-2012>, 2012.

Yadav, D. S., Mishra, A. K., Rai, R., Chaudhary, N., Mukherjee, A., Agrawal, S. B., and Agrawal, M.: Responses of an Old and a Modern Indian Wheat Cultivar to Future O₃ Levels: Physiological, Yield and Grain Quality Parameters, *Environmental Pollution*, 263, 113939, <https://doi.org/10.1016/j.envpol.2020.113939>, 2020.

Sitch, S., Cox, P. M., Collins, W. J., and Huntingford, C.: Indirect Radiative Forcing of Climate Change Through Ozone Effects on the Land-Carbon Sink, *Nature*, 448(7155), 791–795, <https://doi.org/10.1038/nature06059>, 2007.

Tao, F., Feng, Z., Tang, H., Chen, Y., and Kobayashi, K.: Effects of Climate Change, CO₂ and O₃ on Wheat Productivity in Eastern China, Singly and in Combination, *Atmospheric Environment*, 153, 182–193, <https://doi.org/10.1016/j.atmosenv.2017.01.032>, 2017.

Thomson, A. M., Calvin, K. V., Smith, S. J., Kyle, G. P., Volke, A., Patel, P., Delgado-Arias, S. J., Bond-Lamberty, B., Wise, M., Clarke, L., and Edmonds, J.: RCP4.5: A Pathway for Stabilization of Radiative Forcing by 2100, *Climatic Change*, 109(1–2), 77–94, <https://doi.org/10.1007/s10584-011-0151-4>, 2011.

Triboi, E., and Triboi-Blondel, A. M.: Productivity and Grain or Seed Composition: A New Approach to an Old Problem - Invited Paper, *European Journal of Agronomy*, 16(3), 163–186, [https://doi.org/10.1016/S1161-0301\(01\)00146-0](https://doi.org/10.1016/S1161-0301(01)00146-0), 2002.

Wallach, D.: Crop model calibration: A statistical perspective. *Agronomy Journal*, 103(4), 1141–1153. <https://doi.org/10.2134/agronj2010.0432>, 2011.

Wang, Q. J.: Using Genetic Algorithms to Optimise Model Parameters, *Environmental Modelling and Software*, 12(1), 27–34, [https://doi.org/10.1016/S1364-8152\(96\)00030-8](https://doi.org/10.1016/S1364-8152(96)00030-8), 1997.

Yang, L., Liu, S., Tsoka, S., and Papageorgiou, L. G.: Mathematical Programming for Piecewise Linear Regression Analysis, *Expert Systems with Applications*, 44, 156–167, <https://doi.org/10.1016/j.eswa.2015.08.034>, 2016.

Zhang, X., Xu, W., Zhang, G., Lin, W., Zhao, H., Ren, S., Zhou, G., Chen, J., & Xu, X. (2023). First long-term surface ozone variations at an agricultural site in the North China Plain: Evolution under changing meteorology and emissions. *Science of The Total Environment*, 860, 160520. <https://doi.org/10.1016/j.scitotenv.2022.160520>, 2023.

Zheng, B., Chenu, K., Doherty, A., and Chapman, S.: The APSIM-Wheat Module (7.5 R3008), APSIM Initiative, 44 pp, 2015. Available at: <https://www.apsim.info/documentation/model-documentation/crop-module-documentation/wheat/>.

Zhu, X., Feng, Z., Sun, T., Liu, X., Tang, H., Zhu, J., Guo, W., and Kobayashi, K.: Effects of Elevated Ozone Concentration on Yield of Four Chinese Cultivars of Winter Wheat Under Fully Open-Air Field

Conditions, *Global Change Biology*, 17(8), 2697–2706, <https://doi.org/10.1111/j.1365-2486.2011.02400.x>, 2011.

Acknowledgments

We acknowledge the financial support of the Science and Technology Facilities Council (STFC) Research Grant (ST/V002481/1) for the "Pollution and Climate Smart Agriculture in China (PaCSAC)" project which supported initial development of the DO₃SE-Crop model. Support from the Royal Society through the International Exchanges 2021 Cost Share (NSFC) grant (IEC\NSFC\211154) facilitated the UK-China collaboration to parameterise the DO₃SE-Crop model within the project "Understanding the role of air pollution and climate on staple crop yields and nutrition in China". We also received support from STFC Research Grant (ST/Y005317/1) under the EO4AgroClimate programme for the project "Towards a digital twin of cropping systems based on ingestion of EO into process-based crop models" which helped refine the DO₃SE-Crop model for a broader set of country applications.

We would also like to thank the anonymous reviewers for their insightful comments and suggestions, which helped clarify and improve the quality of this manuscript.